

# A Review -Observations of Turbulence and Structure in Magnetized Plasmas

Akihide FUJISAWA

*Advanced Fusion Research Center, Research Institute for Applied Mechanics and Itoh Research Center for Plasma Turbulence, Kyushu University, Kasuga-kouen 6-1, Kasuga, Fukuoka 816-0812, Japan*

(Received 7 May 2010 / Accepted 26 August 2010)

Magnetized plasma is a non-equilibrium matter rich in nonlinear phenomena; its structural formations are dominated by turbulence. This article provides a brief review of experiments and observations of phenomena occurring in turbulent plasmas, with an emphasis on the methodologies for characterizing turbulence, and visualizing the invisible structure created by turbulence and the internal couplings between the elemental waves that constitute turbulence. Zonal flows, streamers, blobs, and other phenomena are investigated by using analytical methods such as Fourier transformation, wavelet analysis, probabilistic density function analysis, bicoherence, wavelet bicoherence. Finally, the contemporary view of plasma turbulence is presented with discussion of unsolved transport issues in fusion plasmas, such as transport barrier formation and nonlocal transport.

© 2010 The Japan Society of Plasma Science and Nuclear Fusion Research

Keywords: turbulence, mesoscale and quasi-coherent structures, energy transfer between turbulence elements, transport barrier formation, zonal flow paradigm, non-local transport

DOI: 10.1585/pfr.5.046

## 1. Introduction

Turbulence is a ubiquitous phenomenon widely observed in nature, therefore, it is important for physical understanding of our surroundings (e.g., the sun, aurora, the ionosphere, dynamos, etc.) and for the modern technologies (e.g., nuclear fusion, plasma displays, plasma rockets, carbon nano-tubes, etc.). In particular, turbulence is a key element for realizing a sun on the earth, i.e., for nuclear fusion based on magnetically confined plasma, since turbulence should determine the plasma's performance, i.e., its basic plasma parameters; confinement time, density and temperature. Therefore, extensive studies of plasma turbulence have been conducted in fusion research from its infancy [1, 2].

The exhaustive studies of plasma turbulence have extended our view of it and yielded insight into turbulence-associated structural formation in magnetized plasmas, such as transport barriers and zonal flows, while simultaneously stimulating the further investigations of the remaining unsolved issues. Our understanding of plasma transport have been extended by the discovery of zonal flows, which regulate plasma turbulence, and of short-lived quasi-coherent structures created by plasma turbulence, such as blobs and streamers. The presence of mesoscale structures has become obvious and their important roles in turbulence and transport have been recognized, establishing the modern view of the plasma turbulence [3–5]. Disparate-scale interaction, such as those between zonal flows (mesoscale) and drift waves (micro-scale) should be highlighted in the discussion of the plasma transport and structural forma-

tion.

These findings and discoveries have been enabled by recent development in diagnostic techniques and methods of analyzing turbulence. Advanced diagnostics have contributed in measuring the electric field or flows in the high-temperature core of turbulent plasmas, leading to the discovery of the zonal flows and geodesic acoustic modes (GAMs). In addition, with the remarkable development of modern computer technology and tools for analysis, we can treat a significant amount of turbulence data and perform the calculations that quantify hidden properties such as nonlinear couplings between elemental components in plasma turbulence. A deeper understanding of plasma turbulence has also been enhanced by small or medium size devices that provide a good environment for physical experiments that cannot be realized in high-temperature devices.

The paper reviews the turbulence experiments in magnetized plasmas in light of the turbulence analysis tools that have furthered progress in plasma physics and controlled fusion. It consists of five sections in addition to this introduction. The following section (Sec. 2) describes fundamental tools and methods for analyzing turbulence, such as Fourier spectral transformation, wavelet, and probability density function (PDF). Section 3 introduces the analytical methods used to visualize coherent structure hidden in turbulence, particularly mesoscale structures, such as zonal flows, streamers, blobs, and repetitive magneto-hydrodynamic phenomena. Section 4 describes the methods for elucidating the interactions between turbulence elements, or components at disparate scales. Section 5 dis-

author's e-mail: fujisawa@triam.kyushu-u.ac.jp

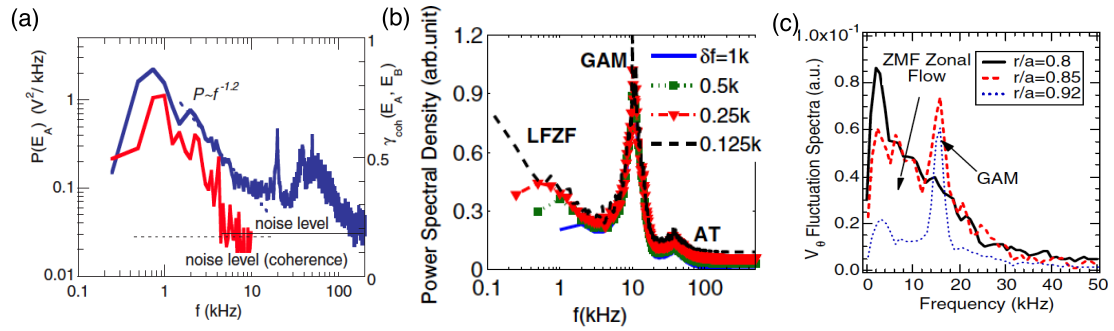


Fig. 1 Examples of fluctuations spectra. Spectrum of (a) electric field in the plasma core of CHS measured with HIBPs (Fig. 1, [9]), (b) that of potential fluctuations at the edge of HL-2A measured with Langmuir probes (Fig. 2, [10]), and (c) that of velocity field fluctuations at the edge of DIII-D measured with beam emission spectroscopy (Fig. 4, [11]). The fluctuation spectra demonstrate the presence of three components of plasma turbulence, drift wave turbulence, zonal flows and GAMs.

cusses synthetic physical issues that extend beyond the issues described in Secs. 2-4, such as flux and flow generation due to turbulence, transport barrier formation, the roles of mesoscale structures (e.g., zonal flows and streamers), and nonlocal transport with respect to disparate-scale interactions. Finally, a brief summary in Sec. 6 indicates future directions.

## 2. Characterization of Turbulence

### 2.1 Spectral decomposition of turbulence - frequency

Fourier spectral analysis is the most popular method for characterizing turbulence. The method decomposes turbulence into a set of elemental waves in the form of sinusoidal functions. The elemental components of turbulence should be labeled by a set of conjugate parameters of space and time, i.e., wavenumber  $k$  and frequency  $f$ . In typical plasma experiments, however, turbulence measurements are performed at a single spatial position with a number of diagnostics, for example, a Langmuir probe, wave scattering, reflectometers [6], and heavy ion beam probes (HIBPs) [7], etc. (for review, see [8]).

In such single-point measurements, the spectral analysis can be applied only to a temporally sequential signals, therefore, the resultant spectra are limited to the frequency domain. Temporally sequential data are written in the Fourier transformation form, as

$$u(t) = \sum_{\omega} \tilde{u}(\omega) \exp(-i\omega t) \Delta\omega. \quad (1)$$

The square of the Fourier coefficient,  $S(\omega) = |\tilde{u}(\omega)|^2$ , indicates the fractional power at a relevant fluctuation element in turbulence, and the power spectrum is calculated statistically by the ensemble average of the auto-powers,

$$\bar{S}_{\text{auto}}(\omega) = \langle |\tilde{u}(\omega)|^2 \rangle = \sum_{i=1}^{N_{\text{ens}}} |\tilde{u}_i(\omega)|^2 / N_{\text{ens}} \quad (2)$$

where  $N_{\text{ens}}$  is the number of realizations.

To date, a number of experimentally obtained spectra have been available, in particular, those of density and potential fluctuations in the frequency domain. The spectra have been found to show turbulence nature of broad band,  $\Delta f/f > 1$  [1, 2]. Spectra of the electric field or velocity fluctuations have recently become available owing to developments in plasma diagnostic techniques and increasing interests in flow structure in toroidal plasmas. Figure 1 illustrates, for example, the spectra of the electric field measured with an HIBP in Compact Helical System (CHS) [9], of potential fluctuations at the edge of HL-2A measured with a Langmuir probe [10], and of velocity fluctuations measured with beam emission spectroscopy (BES) in DIII-D [11].

Similar to those of traditional density fluctuations, these spectra show broad-band features. Further comparison between three spectra, however, shows similarity, or universality. The dominant fraction in the low frequency range connecting to the broad-band fluctuations at higher frequency is superposed on sharp peaks in a range of a few dozen kHz. Recent studies of plasma turbulence show that the spectrum should consist of three major components; stationary zonal flows (low frequency), GAMs (sharp peaks) and drift waves (broad-band). The universality of flow or electric field fluctuations supports the modern view that the turbulence level is determined by interaction between zonal flows (including GAMs) and drift waves, and that the partition ratio between them is crucial to plasma transport.

### 2.2 Spectral decomposition of turbulence - wavenumber

The wavenumber can be directly measured with a few diagnostics such as microwave scattering in which the signal directly indicates the fluctuations at a particular wavenumber, i.e.,  $u(k, t)$  [12, 13]. Fourier spectral analysis in the wavenumber domain is rarely possible in high-temperature plasmas, in contrast to Fourier analysis in the frequency domain, since such analysis requires multispa-

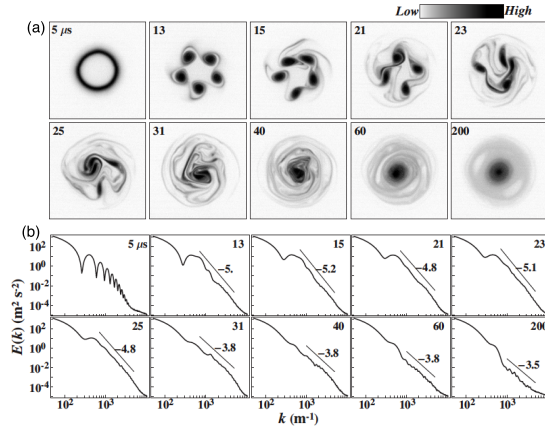


Fig. 2 Structural evolution of 2D pure electron plasma. (a) Relaxation of the density profile from an initial unstable ring shape to a bell shape. (b) Corresponding Fourier spectral evolution in wavenumber space (Figs. 2 and 5, [14]).

tial point measurements. Recently, several imaging techniques, using high-speed cameras, have been well developed that make such spectral analysis in the wavenumber domain possible by using the obtained images of spatial structure.

In this section, an example is presented using pure electron plasma in a laboratory experiment at Kyoto University [14–16]. The relaxation process was observed for an initially unstable distribution of two-dimensional (2D) pure electron plasma trapped in a potential well. Figure 2(a) shows the structural evolution of the pure electron plasma whose density distribution is ring-shaped in unstable equilibrium at the initial stage and then begins to settle into the relaxed state with a bell-shaped distribution through turbulent structural deformation as areas of high-density undergo several merging processes. Each image during relaxation is transformed into Fourier wavenumber space, and the corresponding spectra are shown in Fig. 2(b). The observed decay index of the wavenumber  $\alpha$ , which is defined as  $P(k) \propto k^{-\alpha}$ , is approximately 5 in the early phase and decreases to 3.5 [14, 15];  $\alpha = 3$  is theoretically predicted for uniform 2D turbulence [17, 18]. Later analysis using orthogonal wavelets [16] proved that the decay index of filamentary components should be ( $\alpha = 3$ ) consistent with the theoretical prediction. Moreover, the energy, density, and angular momentum are observed to be conserved whereas clear decay in the enstrophy and the palinstrophy is confirmed in this experiment.

The decay index of the slope in fluctuation spectra characterizes the properties of turbulence and is often associated with its dimensional characteristics. Kolmogorov's five-thirds law,  $P(k) \propto k^{-5/3}$ , is expected to apply in three dimensional (3D) uniform turbulence, while  $P(k) \propto k^{-3}$  is expected for 2D turbulence in the wavenumber. On the other hand, in the frequency domain, the fluctuation spectra obeying  $P(f) \propto f^{-1}$  are ubiquitous in nature. The fa-

mous model of self-organized criticality (SOC) was proposed to explain the universal nature of the  $f^{-1}$  spectra [19]. A review is available on the self-organization of turbulent matter, fluids, and plasmas, which obeys the partial differential equations such as the Navier Stokes and magnetohydrodynamics (MHD) [20].

### 2.3 Full spectral decomposition of turbulence - frequency and wavenumber

Turbulence evolves in space and time, therefore, signals should be transformed simultaneously in wavenumber and frequency. Thus, the Fourier expansion of turbulence field is expressed as

$$u(\vec{r}, t) = \sum_{\vec{k}, \omega} \tilde{u}(\vec{k}, \omega) \exp(i\vec{k} \cdot \vec{r} - \omega t) \Delta\omega \Delta k, \quad (3)$$

where  $\tilde{u}(k, \omega)$  is a complex coefficient function. The strength of each component is expressed by the square of the Fourier coefficient,  $S(\vec{k}, \omega) = \langle |\tilde{u}(\vec{k}, \omega)|^2 \rangle$ .

To evaluate the wavenumber, multichannel detection of fluctuations at various spatial points is essential. This requirement is mostly satisfied in low-temperature laboratory plasmas using Langmuir probe measurements. For instance, in linear cylindrical devices, such as the Kiel Instruments for Wave Investigation (KIWI) [21] and the Large Mirror Device Upgrade (LMD-U) [22, 23] and a toroidal device, TJ-K [24], the Langmuir probe arrays surrounding the plasma surface in the azimuthal direction are used to measure both the spatial and temporal evolution of fluctuations.

Figure 3(a) shows an example of 2D Fourier spectra,  $S(k_\theta, \omega)$ , measured with a 64 channel azimuthal probe array in an LMD-U linear cylindrical plasma [25–27]. Here, the power spectrum can be defined by the ensemble average of the auto-powers as  $\bar{S}_{\text{auto}}(k_\theta, \omega) = \langle |\tilde{u}(k_\theta, \omega)|^2 \rangle$ . It has been reported that the spectral characteristics of linear cylindrical plasmas (produced by Helicon waves) should vary as a function of magnetic field strength and introduced gas pressure. Argon is used, and the pressure and magnetic field strength are  $\sim 0.2$  Pa and 0.1 T, respectively.

From the diagram of  $S(k_\theta, \omega)$ , one of the most fundamental wave characteristics, the dispersion relation, is evaluated using the following formula, as

$$\bar{k}_\theta(\omega) = \sum_{k_\theta} k_\theta S(k_\theta, \omega) / \sum_{k_\theta} S(k_\theta, \omega). \quad (4)$$

When comparing the observed and theoretical dispersion relations, it must be remembered that the plasma should rotate in the laboratory frame causing a Doppler shift in the observed frequency,  $\omega_{\text{obs}} = \omega_0 + k_\theta v_\theta$ . As a result, the measured dispersion relation in the LMD-U is found to be consistent with that evaluated in a linear calculation considering the background plasma rotation (or the Doppler effect).

The two-point correlation technique has been proposed to evaluate the wavenumber spectrum,  $S(k, \omega)$ , in

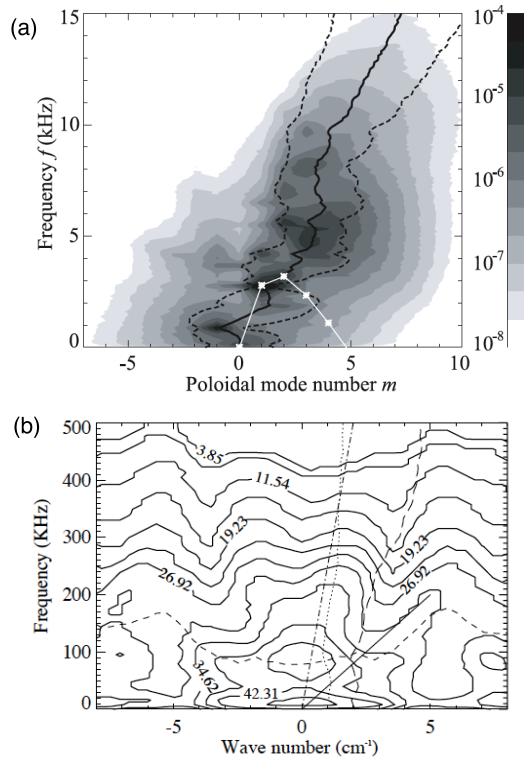


Fig. 3 (a) Fluctuations spectrum  $S(k, \omega)$  in frequency and wavenumber domains. Spectrum is measured with a 64 channel azimuthal probe array in a linear cylindrical plasma, the LMD-U (Fig. 3, [27]). (b)  $S(k, \omega)$  obtained on the low field side in a toroidal plasma, TEXT Upgrade (TEXT-U). Spectrum shows the presence of two modes with phase velocities of  $6.3 \times 10^3$  m/s and  $2 \times 10^3$  m/s at 175 kHz (Fig. 4, [29]).

spatial point measurements from at least two channels. In this technique, the phase difference in signals from the two adjacent points is obtained as a function of frequency in the form,

$$\begin{aligned} P_{\text{crs}}(\omega) &= \langle u(r + \Delta r, \omega) u^*(r, \omega) \rangle \\ &= |P_{\text{crs}}| \exp(i\theta) \\ &= \sqrt{P_{r+\Delta r}(\omega) P_r(\omega)} \gamma_c \exp(i\theta(\omega)), \end{aligned} \quad (5)$$

where  $\theta(\omega)$  is the phase difference between the two adjacent points,  $P_{\text{crs}}(\omega)$ ,  $P_r(\omega)$  and  $P_{r+\Delta r}(\omega)$  are the cross power spectrum of a certain physical quantity,  $u(r)$ , (density, potential, and so on), and the autopowers at the point  $r$  and  $r + \delta r$ , respectively, with  $\gamma_c$  being the coherence between two points. The phase indicates the delay in the wave propagation (and direction) between the two positions. Therefore, the wavenumber can be evaluated by calculating  $k(\omega) = \theta(\omega)/d$ , where  $d$  is the distance between two adjacent positions.

Using the two point correlation technique, one can obtain a wavenumber for a frequency from a single realization, and can produce a histogram if a sufficient number of realizations are available. The resulting histogram is

thought to represent the wavenumber spectrum, and the dispersion relation can be evaluated using Eq. (4). In experiments of cylindrical devices, the dispersions deduced from multipoint measurements and by two-point correlation technique have been compared [21, 22]. The results indicate good agreement when the dispersion relation is simple and monotonic.

In toroidal plasmas, phase contrast imaging (PCI) technique [28] allows us to evaluate the fluctuation spectrum in the wavenumber and frequency domains. Figure 3 (b) shows the complete density fluctuation spectrum in the frequency and wavenumber domains in the interior of the TEXAS Experimental Tokamak (TEXT) plasma measured with PCI technique [29]. The results reveal the existence of two distinctive branches of the dispersion relation, which can resolve the existing puzzling discrepancy between the dispersion relations measured with an HIBP and with the microwave scattering method. The discrepancy is ascribed to the difference in the sensitivity between the two diagnostics, that is, the HIBP is more sensitive to low wavenumbers, so the evaluated dispersion relation corresponds to the branch with faster phase velocity, whereas the microwave scattering is highly sensitive to higher wavenumbers.

## 2.4 Wavelet analysis for intermittency

Turbulence is not stationary but dynamic, however, the Fourier analysis itself has no power to resolve the time-dependent nature of turbulence. This is a serious drawback in the use of Fourier analysis to investigate the dynamics of turbulence and coherent modes, the mutual interaction between the elemental waves in turbulence, common features of turbulence, i.e. intermittency, and so on. Other methods are needed to study the time-dependent nature of turbulence.

The wavelet transformation, which is mathematically regarded as a set of extended numerical filters, offers a sophisticated approach to investigate the dynamic nature of turbulence. Numerical filtering is a standard technique for extracting a component of a particular frequency range from a given data sequence. The general definition of the numerical filter is expressed as

$$g(t) = \int_{-\infty}^{\infty} h(t - t') f(t') dt', \quad (6)$$

where  $f(t)$ ,  $g(t)$  and  $h(t)$  represent a given waveform, the filtered waveform, and the kernel of the numerical filter, respectively [30]. Wavelet transformation is defined as a set of filter functions,  $h(a, t)$ , where  $a$  is the identical parameter of each wavelet basis. The wavelet is a tool to obtain both time and frequency resolutions, which could be regarded as a sophisticated version of a short-term Fourier transform.

The Morlet wavelet is widely used in the analysis of plasma turbulence, since it is considered as an extension of traditional Fourier analysis. In the Morlet wavelet trans-

form, the kernel function is written as

$$h(a, t) = a^{-1/2} \exp[i2\pi t/a - (t/a)^2/2], \quad (7)$$

maintaining a correspondence with the traditional Fourier spectral analysis. In the wavelet transformation, the parameter  $a$  corresponds to the inverse of the frequency, that is,  $\omega = 2\pi/a$ . Therefore, the Morlet wavelet is considered as a natural extension of the Fourier analysis that offers a reasonable compromise between frequency and temporal resolution. However, it is not a true wavelet in the strictly mathematical sense, because the Morlet wavelet basis does not possess the orthogonal conditions that a mathematically true wavelet should satisfy.

The time-dependent nature of turbulence can be visualized using wavelet analysis. Figure 4 shows an example of the wavelet analysis of electric field fluctuations observed with an HIBP in CHS [9]. The temporal evolution of the fluctuation spectrum in Fig. 4(a) demonstrates the quasi-periodic variation in the integrated fluctuation amplitude around  $\sim 50$  kHz. The variation frequency should be almost consistent with the frequency of stationary zonal flows,  $Z_A(t)$ ; the waveform of the stationary zonal flows is shown in Fig. 4(b). Note that the zonal flow waveform is extracted using a band-pass filter (see the definition in Sec. 3.4). Figure 4(c) shows the power spectrum of the envelop of the integrated fluctuation power at 30–100 kHz. The power spectrum shows, in fact, a sharp peak at  $\sim 0.5$  kHz, which is consistent with the zonal flow frequency. It is confirmed that the integrated fluctuation power at 30–100 kHz should be modulated by the zonal flows (see Fig. 4(d)).

To clarify how the zonal flows modulate the turbulence, the electric field fluctuation spectra are conditionally averaged with the zonal flow maxima and minima. Here, at the maxima, the zonal flow speed is highest in the direction of the bulk plasma flows. The result shows a clear difference, i.e., the fluctuation power around  $\sim 50$  kHz is lower at the maximum of zonal flows than that at the minimum of zonal flows. The turbulence characteristics are found to be changed or affected by the state of zonal flows. Note that the changes in zonal flows occur approximately 100 times slower than the microscale fluctuations. Therefore, the zonal flows could be the background structure regulating the broad-band fluctuations. The combined use of the Morelet wavelet with the conditional average technique successfully reveals a hidden property of turbulence that cannot be elucidated by Fourier transformation.

Finally, a few example of the analysis using the true wavelets in the mathematical sense can be given. The usage of such wavelet was proposed as a method of decomposing the turbulence signals to coherent and incoherent (or noise) components, with a suggestion that the plasma transport should be induced by the coherent component [31]. Moreover, an orthogonal wavelet was applied to spatially structural analysis in the pure electron plasmas shown in Fig. 2, and successfully removed the noise

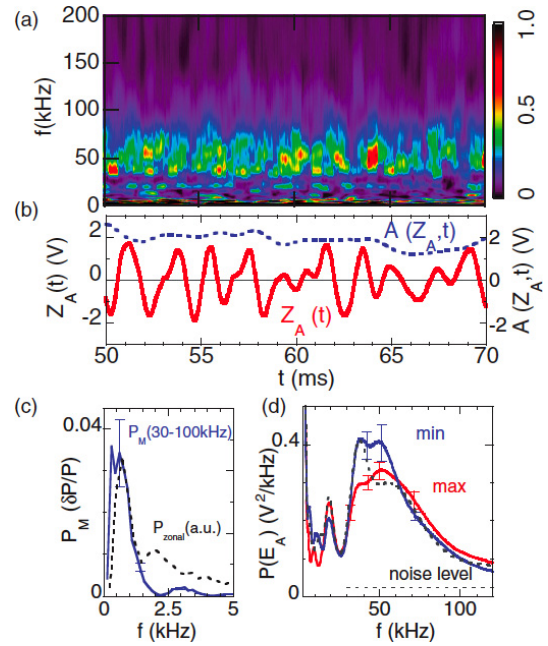


Fig. 4 Turbulence modulation due to stationary zonal flows in CHS. (a) Temporal evolutions of wavelet spectrum of electric field fluctuations defined as  $\Delta\tilde{\phi} = \tilde{E}\Delta r$ , where  $\Delta r$  is the distance between the two spatial channels. Color bar uses units of  $V^2 \text{ kHz}^{-1}$ . (b) Evolution of the zonal flows,  $Z_A(t)$ . Waveform of the zonal flow is the electric field numerically filtered in the frequency range around 0.5 kHz. Blue dashed line indicates the evolution of zonal flow amplitude using wavelet analysis,  $\text{Env}[Z_A; t]$ . (c) FFT spectrum of wavelet power modulation in the frequency range from 30 to 100 kHz,  $P_M$ . Black dashed line,  $P_{zonal}$ , represents the electric field fluctuation in the zonal flow range for comparison. (d) Conditional averages of wavelet power spectra around the local maxima and minima of the zonal flow. Grey dashed line represents the conditional averaged spectrum when  $Z_A(t) \approx 0$  (Fig. 2, [9]).

in high wavenumber components, without any distortion of the ‘signals’. This achievement made it possible to find that the real decay index of the energy spectrum should obey the theoretical prediction [16], as shown in Sec. 2.2.

## 2.5 Probability density function analysis for nonlinearity

The other fundamental method for extracting turbulence properties is a statistical approach for evaluating the probability density function (PDF) of the fluctuation height of a variable. If the fluctuations are simply expressed as a superposition of individual modes with random phases, the central limit theorem guarantees that the corresponding PDF of the fluctuations should have a Gaussian distribution. Therefore, the deviation of the PDF from the Gaussian indicates the degree of mutual dependence or the memory effects of variables, that is, the degree of the internal nonlinearity of the turbulence. Because this deviation

suggests the presence of coherent structure in the plasma, it can be considered a measure of the degree to which structured fluctuations are present. The degree of deviation from the Gaussian can be used as a parameter that expresses the way the structured fluctuations are buried in turbulence.

The first application of the PDF analysis to plasma turbulence was made in the ADITYA tokamak [32] after the study of intermittency in turbulent fluids [33, 34]. To date, a number of trials to classify and compare the turbulent characteristics have been conducted by constructing the PDF of plasma turbulence [35–43]. The usage of the PDF method may be encouraged after the plasma transport model based on SOC [44], since the SOC model predicted the scale-invariant characteristics that could be evaluated statistically.

Several comparisons of the statistical characteristics have been conducted to clarify the universality, for instance, between the edge turbulence in toroidal plasmas (including tokamaks and stellarators) and that in cylindrical devices [35, 42, 45]. Figure 5 is an example of a trial that investigated the similarity in the turbulence characteristics at the center and periphery of a linear cylindrical plasma, PISCES, and in the scrape off layer (SOL) in a tokamak, Tore Supra. The density fluctuations at both the periphery in PISCES and the SOL in Tore Supra shows a high degree of nonlinearity or a clear deviation from of a Gaussian distribution, whereas that in the center shows a Gaussian characteristics suggesting a random distribution. The strong deviation from the Gaussian at the periphery in PISCES and the edge in Tore Supra is ascribed to the generation of mesoscale structure that enhances radial transport, called *avoids*, which is probably the same phenomenon as blobs (discussed again in Sec. 3.4).

The deviation from the Gaussian can be quantitatively evaluated with several moments of the PDF, for example,

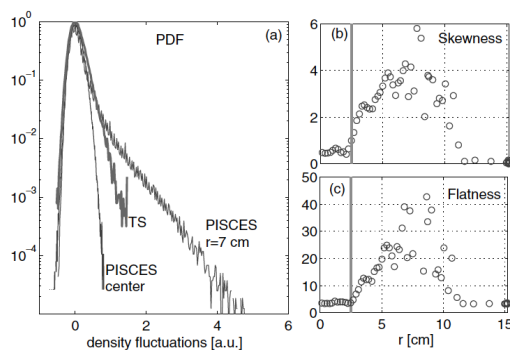


Fig. 5 (a) Usage of PDF analysis to compare the turbulence characteristics in the SOL of Tore-Supra and those at the center and edge of a linear cylindrical plasma, PISCES. (b) Skewness and (c) kurtosis are shown as a set of scalars to characterize the PDFs for the PISCES. Vertical lines represent the plasma edge (Fig. 5, [45]).

the third and fourth moments, called skewness and kurtosis, respectively. Skewness and kurtosis are defined as

$$s = \int_{-\infty}^{\infty} (\tilde{\phi} - \mu)^3 P(\tilde{\phi}) d\tilde{\phi} / \sigma^3, \quad (8)$$

$$k_u = \int_{-\infty}^{\infty} (\tilde{\phi} - \mu)^4 P(\tilde{\phi}) d\tilde{\phi} / \sigma^4, \quad (9)$$

respectively, where  $\mu$  and  $\sigma$  are the first (average) and second moments (variance) of the PDF, respectively, explicitly expressed as,

$$\mu = \int_{-\infty}^{\infty} \tilde{\phi} P(\tilde{\phi}) d\tilde{\phi} \quad (10)$$

$$\sigma^2 = \int_{-\infty}^{\infty} (\tilde{\phi} - \mu)^2 P(\tilde{\phi}) d\tilde{\phi} \quad (11)$$

Note that  $s = 0$  and  $k_u = 3$  for a complete Gaussian distribution [37]. Figures 5 (b) and 5 (c) shows the skewness and kurtosis as a function of radius in PISCES. The result indicates that the degree of nonlinearity should increase at a radius of less than  $r \approx 10$  cm, while at the outer radius of  $r \approx 10$  cm the fluctuations are dominated by noise.

Like the turbulence signals observed in potential and density in a number of experiments, the transport associated with turbulence should be intermittent [36, 46]. The PDF analysis can be used to clarify the nature of turbulence-driven transport. Figure 6 (a) presents the results of an early trial to evaluate the turbulence-driven particle transport at the plasma edge of the Axially Symmetric Divertor Experiment (ASDEX) tokamak [36]. The temporal evolution clearly indicates the presence of intermittent positive bursts of particle flux. PDF analysis of the temporal value of the flux reveals that both positive and negative values are possible, with most of values being near zero. Moreover, the positive tail components of the fluxes, surprisingly, contributes to the outward particle transport; half of the outward flux occurs in the positive bursts with its amplitudes three times larger than the mean value. Therefore, the turbulence driven particle flux is strongly structured to govern the transport at the plasma edge.

A combination of wavelet and PDF analysis reveals the variation in the fluctuation properties with the frequency, or the variation in the degree of nonlinearity with the frequency. Figure 6 (b) shows the PDFs of the particle flux density as a function of frequency ( $n_e = 1.2 \times 10^{17} \text{ m}^{-3}$  and  $T_e(0) = 10 \text{ eV}$ ) in the TJ-K stellarator [24, 47]. The particle flux is analyzed by using the Morelet (and Mexican hat) wavelets in a helium plasma. The intermittency is characterized for each wavelet component of the frequency, by calculating the kurtosis,  $k_u(f)$ . The results show three characteristics regimes; i) the Gaussian transport regime,  $k_u \approx 0$ , of low frequency less than  $\sim 10$  kHz, ii) an intermediate intermittent regime,  $k_u \approx 2$ , of less than 80 kHz, whose power decays as  $P \propto f^{-1}$  corresponding to the characteristics of SOC, and iii) the strong intermittent regime, up to  $k_u \approx 20$ , of higher frequency above  $\sim 100$  kHz, where the spectrum shows a decay as

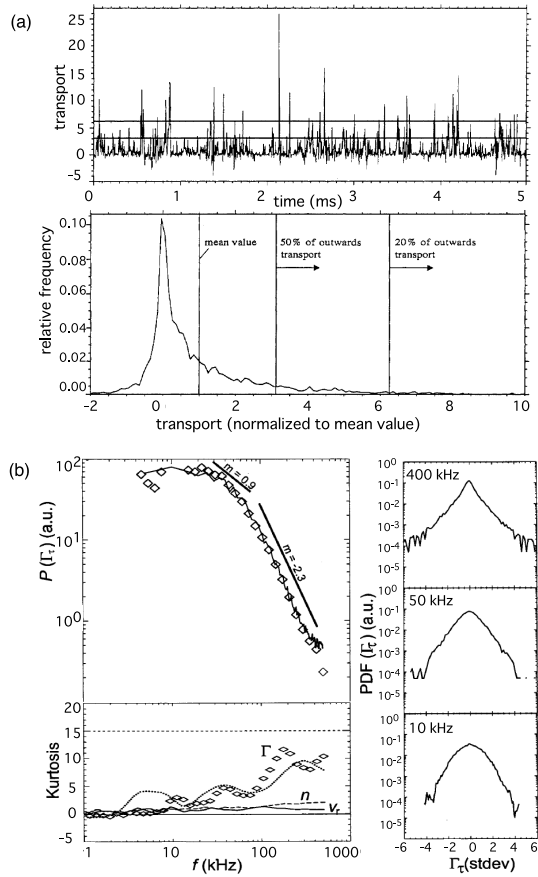


Fig. 6 (a) Turbulence-driven particle flux as a function of time, and probability density functions of the flux at the edge of a tokamak plasma, ASDEX. The turbulence-driven particle flux is evaluated using  $\vec{E} \times B$  drift and density fluctuations (Figs. 7 and 8, [36]). (b) Examples of the combined PDF and wavelet analysis. (upper) Power spectra of experimentally evaluated particle flux in TJ-K. Wavelet and Fourier power spectra are represented by diamonds and a solid line, respectively. (lower) Kurtosis of the wavelet transformed data as a function of frequency. Higher-frequency fluctuations (above  $\sim 100$  kHz) are characterized by a strong intermittency (Fig. 3, [47]).

$P \propto f^{-5}$ . Consequently, this combined PDF/wavelet analysis reveals the variation in the fluctuation structure for frequency regimes.

### 3. Extraction of Coherent Structure from Turbulent Background

#### 3.1 Conditional average and drift eigenmode structure

A number of intermittent, catastrophic, short-lived and transient but quasi-coherent and quasi-periodic structures often appear in turbulence plasmas, e.g., blobs, streamers, sawtooth phenomena. These phenomena can be probabilistic, and are often buried in the background turbulence. Their short-lived nature makes it difficult to elucidate the structures' spatiotemporal evolution precisely

without multipoint measurements covering the region in which the phenomena occur. However, assuming a certain degree of reproducibility of the events, the conditional statistical average provides a way to deduce the most probable evolution of physical quantities at a spatial point if the emergence of the target phenomenon can somehow be detected.

The conditional average is a method of visualizing such probabilistic and reproducible phenomena occurring in a turbulent background. The principle of the conditional average is simple; it uses simultaneous measurements of a physical quantity at two positions. For example, two Langmuir probes are used to measure the space potentials at two spatial points simultaneously; one probe is fixed at a certain position as the reference to determine the occurrence of the phenomenon, while the other probe is moved two dimensionally. If the reference probe signal at a position  $\vec{r}_0$  has a prescribed value indicating the occurrence of the target phenomenon at a time  $t_i$ , the movable probe signal  $\Phi(\vec{r}, t_i + \tau)$ , simultaneously recorded at a different position at  $\vec{r}$ , is sampled. Then the ensemble average is calculated for statistical independent realizations, and a typical temporal evolution of the signal at  $\vec{r}$  is obtained as

$$\Phi_{CA}(\vec{r}, \tau) = \langle \Phi(\vec{r}, t_i + \tau) \rangle, \quad (12)$$

where  $\Phi_{CA}(\vec{r}, \tau)$  represents the conditional averaged evolution of the spatial pattern of the target phenomenon.

The usefulness of conditional averaging was first demonstrated and discussed in a conventional double-plasma device [48] and a number of instances are available [49–53]. Figure 7 shows an example in which the conditional average is used to deduce the structure of a single drift wave in a linear cylindrical device, the KIWI [50]. Figure 7 clearly shows the 3D evolution of the coherent drift wave structure, which indicates poloidal  $m = 2$  mode structure that is uniform along the magnetic field direction. The patterns were obtained by conditional averaging of 2000–3000 density fluctuation ensembles measured with Langmuir probes.

#### 3.2 Nonlinear evolution of MHD structure

A number of quasi-periodic phenomena associated with MHD instabilities have been observed in toroidal plasmas, such as sawtooth oscillation [54], edge localized modes (ELMs) [55], and fishbone instabilities [56]. These MHD phenomena are appropriate targets for application of the conditional average technique to deduce their typical or averaged structural evolution of them. In the TEXT tokamak the change in electron temperature fluctuations was measured during a cycle of sawtooth oscillation [57]. Here the so-called CHS fishbone [58, 59] is introduced as an example in which the conditional average technique revealed the nonlinear evolution of plasma flows during the quasi-periodic structural changes of this phenomenon.

The CHS fishbone is considered to be a MHD quasi-cyclic oscillation (with a period of  $\sim 3$  ms) driven by

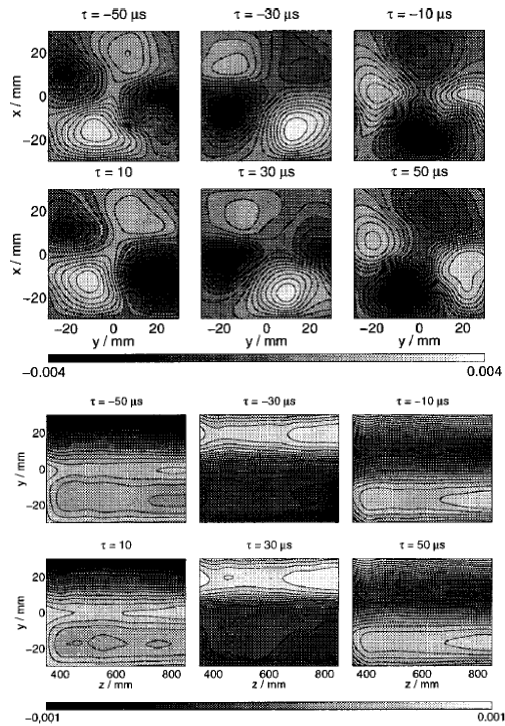


Fig. 7 Drift wave eigenmode structured deduced using the conditional average technique in a linear cylindrical device, the KIWI. (top) Axial view, and (bottom) side view of the plasma (Figs. 3 and 4, [50]).

neutral-beam-injected (NBI) energetic ions. It is observed in NBI heated plasmas with low densities of  $n_e \sim 1 \times 10^{19} \text{ m}^{-3}$ . The phenomenon is dominated by magnetic field distortion associated with an  $m/n = 2/1$  mode, and consists of two phases; the precursor phase characterized by frequency chirping from  $\sim 40 \text{ kHz}$  to  $0 \text{ kHz}$  (rotating in electron diamagnetic direction) and the low frequency post-cursor phase at  $\sim 5 \text{ kHz}$  (rotating in the ion diamagnetic direction). The evolution of the magnetic field distortion and plasma flows associated with this phenomenon was measured with twin HIBPs. The observation point of one HIBP was altered approximately every 5 mm shot by shot, while the other was fixed at a radial position as a monitor. The conditional average technique was applied on about a dozen periods of identical bursts of CHS fishbone.

Figure 8 shows a typical evolution of the equipotentials of electrostatic potential during a CHS fishbone cycle. The patterns are obtained after averaging the signals from more than a dozen identical fishbone bursts, assuming that the bursts consist of  $m = 2$  and  $m = 0$  modes. The equipotential contours reflect the lines of the plasma flows if these plasma flows are expressed by  $E \times B$  drift. In the first phase, the  $m = 2$  mode characteristic is clearly dominant. Then the symmetric oscillatory flows develop toward the second phase of the CHS fishbone ( $t > \sim 1.5 \text{ ms}$ ), and gradually disappears by the end of the cycle ( $t \sim 3 \text{ ms}$ ).

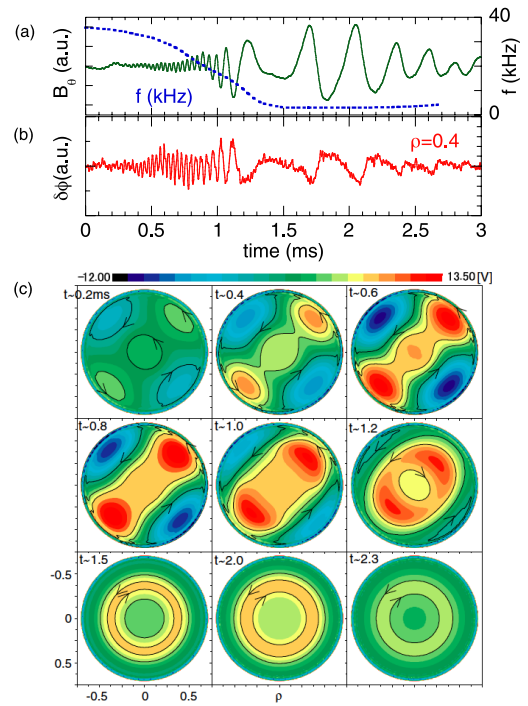


Fig. 8 Temporal evolution of flow patterns associated with CHS fishbone. (a) Magnetic field fluctuation and the accompanying changes in frequency (dashed line). (b) Potential fluctuation signal of an HIBP at  $\rho = 0.4$ . Mode changes from  $n = 1$  to  $n = 0$  during the chirping phase. (c) Reconstructed 2D image plots of potential fluctuation or perturbed flowpattern evolution during a burst;  $t = 0.2, 0.4, 0.6, 0.8, 1.0, 1.2, 1.5, 2.0$  and  $2.3 \text{ ms}$ . Equi-potential contours are equivalent to the fluctuating  $E \times B$  flow pattern (Figs. 1 and 3, [58]).

One of the important finding regarding the flow pattern evolution is that oscillating zonal flows grow to develop sheared structure that may affect the microscale turbulence, although the shearing rate of the oscillatory shear flows found in the CHS experiment is too small to affect the turbulence. The discovery of the oscillatory sheared flows, which is driven by the energetic ions interacting with an MHD mode, should be emphasized, since the resulting electric field shear in future burning plasmas could become sufficiently large to reduce the turbulence transport.

### 3.3 Spatiotemporal evolution of blobs

Blobs are intermittent and coherent structure observed both in linear plasmas and at the periphery regimes of toroidal plasmas. After blobs were first identified in toroidal plasmas by using a 2D Langmuir probe array in the 1980's [60], phenomena identical to blobs have been found, although they were given different names, such as avoloid (see Sec. 2.5) and intermittent plasma objects (IPO) [61, 62]. The phenomena are characterized by sudden intermittent increases or decreases in density, and have been extensively studied, since the blobs are thought to

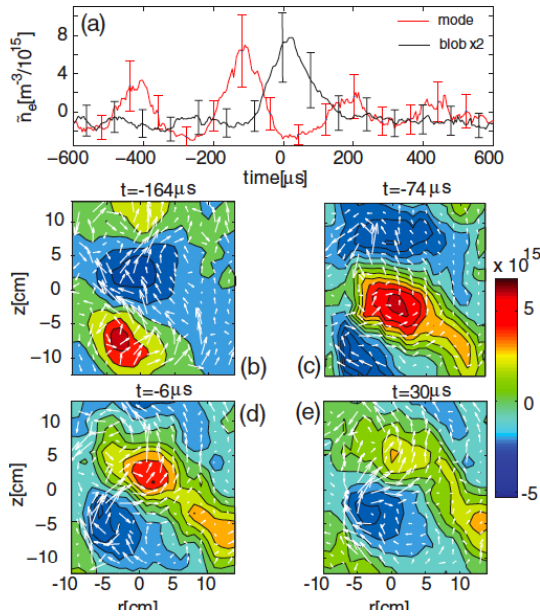


Fig. 9 Blob generation processes deduced by a conditional averaging technique in the TORPEX device. (a) Time history of  $n_e$ , including uncertainties, in the mode region (red) at  $r = 1$  cm,  $z = 5$  cm and in the source-free region (black) at  $r = 13$  cm,  $z = 5$  cm. Note that the latter is multiplied by two for clarity (Fig. 3, [64]).

govern the transport at the edge and in the SOL of toroidal plasmas.

Recently, the mechanism of blob generation has been investigated using many low-temperature devices in university laboratories, thereby shedding light on edge plasma transport. In particular, the use of conditional average combined with the efficient use of the Langmuir probes has revealed the detailed spatiotemporal evolution of blobs [63, 64]. Figure 9 shows an example of spatiotemporal evolution obtained with this method in the TORPEX device ( $R = 1.0$  m,  $a = 0.2$  m,  $B_t = 76$  mT), which is a toroidal device without an internal plasma current and thus without confinement. The plasma is produced with  $\sim 400$  W microwaves, and the resulting density and electron temperature used in this experiment are approximately  $n_e \sim 1 \times 10^{10}$  cm $^{-3}$  and  $T_e = 4$  eV, respectively.

In this instance, 600 identical blobs are averaged to deduce the spatiotemporal patterns of their evolution. Blobs are assumed to be identical if the increased density fluctuation amplitude (in the ion saturation current) is in the range of  $4.5\sigma_I < \tilde{I}_{\text{ref}} < 4.7\sigma_I$ , where  $I_{\text{ref}}$  and  $\sigma_I$  represent the ion saturation current of the reference probe and its standard deviation of the ion saturation current, respectively. In the spatiotemporal evolution patterns, a radially elongated interchange pattern rotates with  $E \times B$  drift, and then a mass of high dense plasma is sheared off and ejected outward and enhancing radial plasma transport. The observation suggests the importance of interchange instabilities and sheared flow in blob generation.

A cylindrical device named the upgraded Large Plasma Device (LAPD) found that holes (density depletion events, going inward) were generated along with blobs (density enhanced events, going outward). The results indicated that their size should be dependent on the ion sound gyroradius [52]. A similar phenomenon, the paired creation of blobs and holes, was also found in the edge of a toroidal plasma, the Joint European Tokamak (JET), suggesting the energy transfer from these mesoscale structures to zonal flows, which could play a role in saturating the plasma edge turbulence [65]. The spatiotemporal characteristics of blobs have also been observed using 2D diagnostic techniques, such as Langmuir probes [66, 67], gas puff imaging [68], and so on.

### 3.4 Correlation analysis and zonal flow identification

The zonal flows are mesoscale structures that are linearly stable but nonlinearly driven by background waves or turbulence. Their major characteristics of the zonal flows are, i) they are symmetric around the magnetic axis ( $m = n = 0$ ), and ii) they have a mesoscale wavelength in the radial direction ( $k_r \neq 0$ ) [3, 4, 69, 70]. The symmetric pattern of the zonal flows means that they cause no transport, thus, an increase in the zonal flows, caused by the energy transfer from the turbulence, contributes to enhancing the plasma confinement. In toroidal plasmas, two kinds of zonal flows are theoretically predicted; one is called here stationary zonal flows, and the other is GAMs.

The presence of stationary zonal flows and GAMs can appear in the electric field or velocity fluctuation spectra (see Fig. 1). Note that in magnetically confined plasmas, the flow perpendicular to the confinement magnetic field is coupled to  $E \times B$  drift, hence the radial electric field measurement is equivalent to that of the perpendicular flows. In CHS experiments the existence of the zonal flow pattern was confirmed for the first time [71], and the radial pattern of the stationary zonal flows was deduced with a correlation function analysis using two-point measurement of radial electric field fluctuations with dual HIBPs. Figure 10 shows the spatiotemporal pattern of zonal flows inferred in correlation function measurements using twin HIBPs in the CHS stellarator [71, 72].

The correlation function is obtained as follows. First, this CHS experiment showed that the electric field fluctuations ranging from  $\sim 0.5$  to  $\sim 1$  kHz should be symmetrical on the magnetic flux surface. In the analysis, the zonal flow waveform is extracted using a numerical band-pass filter whose kernel is defined by Eq. (6), i.e.,  $Z_A(t) = \int_{t-\infty}^{t+\infty} h(t-t')x(t')dt'$ , where  $h(t-t') = (2\pi\tau_S^2)^{-1/2} \exp[-(t-t')^2/2\tau_S^2] - (2\pi\tau_L^2)^{-1/2} \exp[-(t-t')^2/2\tau_L^2]$ . Here, the short time constant defining the upper limit of the zonal flow frequency is selected as  $\tau_S = 0.3$  ms, while the other is set as  $\tau_L = 1$  ms to remove extremely low frequencies, which may reflect the effects of plasma movement or changes

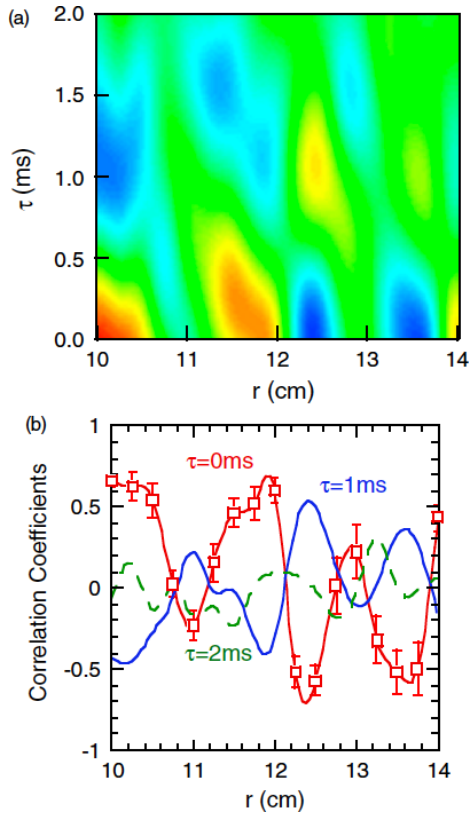


Fig. 10 Zonal flow pattern deduced by cross-correlation technique in CHS stellarator. (a) Spatiotemporal structure of stationary zonal flows evaluated from the correlation function in CHS. (b) Spatial correlation with the time lag of  $\tau = 0, 1$  and  $2$  ms (Fig. 2, [74]).

in the plasma parameters. The resulting filter has a peak around  $0.5$  kHz with a width of  $\sim 1$  kHz in the frequency domain.

After extracting the zonal flow waveform, the spatiotemporal structure of the stationary zonal flow can be inferred by evaluating the correlation function

$$C_{\text{crs}}(r + \rho, t + \tau) = \left\langle T^{-1} \int_{-T/2}^{T/2} \tilde{Z}_A(r, t) \tilde{Z}_A(r + \rho, t + \tau) dt \right\rangle. \quad (13)$$

In the actual experiment, an HIBP observation point was fixed at about half-radius of  $r = 12$  cm while the other location was varied from  $10$  cm to  $14$  cm. The result in Fig. 10 shows that the zonal flows should have a finite radial wavelength of  $\sim 1$  cm, and a life time of zonal flows is  $\sim 2$  ms since the initial pattern would be lost, as is obvious in Fig. 10(b), upon the deformation of the radial correlation function.

To date, a few experiments have been conducted to identify stationary zonal flows [73], for example, the BES was used to search for the signature of the stationary zonal flows in the core ( $0.6 < r/a < 0.8$ ) of the L-mode plasma in DIII-D [11]. Regarding the oscillatory branch of zonal flows (GAMs), solitary GAM peaks

have been found in the fluctuation spectra of a number of toroidal plasmas [74], such as the JIPPT-IIU [75], JFT-2M [76, 77], ASDEX-U [78, 79] T-10 [80], DIII-D [81–83], TEXT-U [84] and CHS [85], after GAMs were identified in the H1-heliac [86]. This is partially because the oscillatory nature of GAMs makes it relatively easier to detect them. In tokamaks, clear GAM peaks are usually observed at the plasma edge. The complete symmetry of GAMs ( $m/n = 0/0$ ) has been confirmed by multichannel Langmuir probes located in both the toroidal and poloidal directions in HL-2A [87, 88] after the initial identification of poloidal symmetry ( $m \sim 0$ ) in many devices. Moreover, the details of density fluctuations accompanying GAMs have been reported by measurements using a correlation reflectometer in the Tokamak Experiment for Technology-Oriented Research (TEXTOR) [89]. Finally, the presence of a zonal magnetic field was confirmed in CHS experiments in a similar analyzing procedure of zonal flow identification [90].

### 3.5 Searches for streamers

Streamers are mesoscale structures nonlinearly generated from drift wave turbulence, as is similar to zonal flows [69]. Unlike zonal flows, the streamers are short-lived structures that are radially elongated and localized in the poloidal direction at mesoscale width, i.e.,  $k_r = 0$  and  $k_\theta \neq 0$ . A number of simulations predicted the existence of streamers [91, 92], and theory predicted that streamers should become dominant as the collisionality increases. Indeed, streamers or a similar kind of nonlinear structure appear to be observed at the plasma edge of fusion-oriented devices, or university-scale laboratory devices where the effective collisionality is high owing to low-temperature and a high fraction of neutrals [93].

Streamers are considered to enhance the cross-field transport, as is likely for the blobs in the plasma periphery. To date, however, a few observations have suggested the signature of streamer formation in toroidal plasma experiments [94, 95], such as in the HIBP measurement in JIPPT-IIU [95], in electron cyclotron emission (ECE) measurements covering a wide radial extent from a normalized radius  $\rho$  of  $0.2$  to  $1.0$  in DIII-D [94]. The DIII-D measurements revealed the presence of intermittent radial elongated structures, lasting for  $2$ - $50$  ms, denoted as *avalanches*, although the “avalanche” may denote an axisymmetric structure ( $m = 0$ ) in the theoretical sense.

In a linear cylindrical plasma, the LMD-U, on the other hand, streamer formation was identified by the efficient use of a combination of a  $64$ -channel azimuthal probe array and a  $2D$  movable probe [26]. The azimuthal probe array found that a poloidally localized structure was generated rather quasi-periodically by nonlinear couplings between elemental drift wave components (up to  $m \sim 6$ , where  $m$  is the poloidal mode number). Figure 11 shows an example of density (ion saturation current) fluctuations

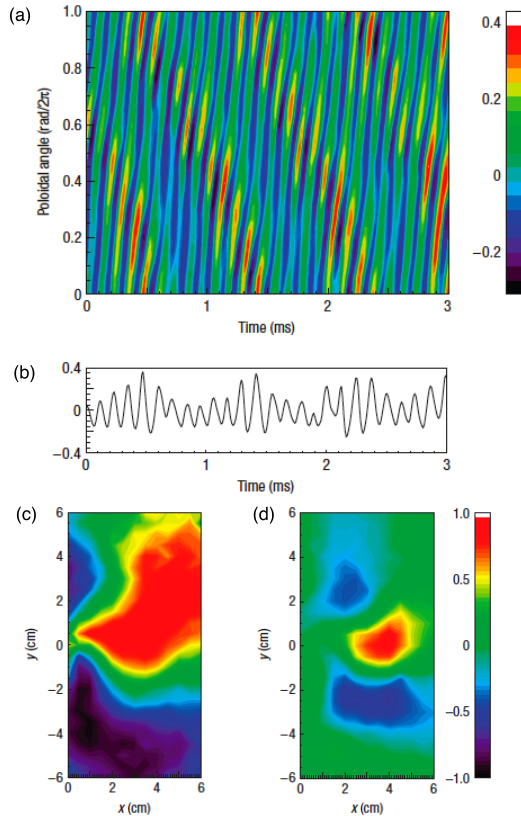


Fig. 11 Time evolution of streamer structures. (a) Simultaneous measurement of the spatiotemporal behaviours of the ion saturation-current fluctuations by 64 channels at  $r = 4$  cm and  $z = 1.885$  m (b) Temporal behaviour of at  $\theta = 0$ . (c) Real parts of cross-spectra between the reference probe [ $(x, y, z) = (4$  cm, 0, 1.625 m)] and the 2D movable probe ( $z = 1.375$  m). Frequency ranges are 7.8 kHz (one of the main components of the streamer), and (d) 10-15 kHz (broadband region) (Figs. 3 and 4, [26]).

detected with the 64-channel probe array, indicating that quasi-periodical bursts are localized in a narrow poloidal region, and that the poloidal localized structure propagates in the opposite direction to the carrier wave ( $m = 1, f = 2.8$  kHz).

The cross-correlation between the potential signals at the two points (Figs. 11 (c) and (d)), using a 2D movable probe as a reference probe, confirmed that the elementary modes that form the streamers should be radially elongated. More detailed analysis suggests that the structure is formed by the bunching of three elemental waves, i.e.,  $(m, f) = (2, 7.8$  kHz),  $(m, f) = (3, 6.6$  kHz) and broadband components up to  $(m, f) = (6, 15$  kHz), which are observed in the turbulent states. Therefore, these analyses conclude that the poloidally localized and radially elongated structure are streamers.

Definite identification of streamers in toroidal plasmas should be an interesting future work. The 2D properties of streamers will make it necessary to develop a wide range of 2D simultaneous measurement radially and poloidally

with sufficiently fine temporal resolution. Although such measurements can be quite difficult, they are essential for identifying streamers and investigating their contribution to transport, and their mutual interactions with zonal flows and turbulence, suggesting another intriguing possibility for plasma experiments.

## 4. Visualization of Internal Turbulence Structure

### 4.1 Bicoherence for quantifying three-wave couplings

The presence of nonlinear dynamics in turbulence could manifest itself in the deviation from the Gaussian distribution in PDF analysis, although such analysis could not reveal the fine structure of the nonlinearity, or the details of the elemental wave couplings. Bispectral or bicoherence analysis can reveal the properties of three wave couplings between elemental wave components contained in turbulence [96, 97]. Bicoherence analysis provided the first evidence of three-wave couplings in broad-band turbulence spectra measured with Langmuir probes at the plasma edge in the Advanced Toroidal Facility (ATF) toratron [98]. Then, the bicoherence analysis was employed to evaluate the nonlinear processes of shear flow generation due to turbulence in both toroidal and cylindrical linear plasmas [99, 100], and its role in the H-mode transition in DIII-D [101]. Recently, bicoherence has been applied to prove that coupling occurs between zonal flows (in particular, GAMs) and turbulence [86, 87, 102]. A theoretical model was proposed to connect the observed bicoherence value with the coupling strength between the waves [103].

The bispectrum is defined by

$$B(\omega_1, \omega_2) = \langle \tilde{f}(\omega_1) \tilde{f}(\omega_2) \tilde{f}^*(\omega_3) \rangle, \quad (14)$$

where  $f(\omega_1)$ ,  $f(\omega_2)$  and  $f(\omega_3)$  represent the Fourier coefficients at the frequencies of  $\omega_1$ ,  $\omega_2$  and  $\omega_3$ , respectively. Bicoherence, the normalized bispectrum, is employed as a measure of the strength of three wave coupling. Bicoherence is defined explicitly as

$$b^2(\omega_1, \omega_2) = \frac{|\langle \tilde{f}(\omega_1) \tilde{f}(\omega_2) \tilde{f}^*(\omega_3) \rangle|^2}{\langle |\tilde{f}(\omega_1) \tilde{f}(\omega_2)|^2 \rangle \langle |\tilde{f}(\omega_3)|^2 \rangle}. \quad (15)$$

The bicoherence indicates phase coherence between three waves of frequencies at  $\omega_1$ ,  $\omega_2$  and  $\omega_3$ , which satisfy the relationship  $\omega_1 + \omega_2 = \omega_3$ . Otherwise, the bicoherence value is automatically zero. If  $\omega_1 + \omega_2 = \omega_3$  is satisfied, the numerator generally takes the form of  $\sum |A_i| \exp(i\delta_i)$ . If the individual waves are independent, the phases  $\delta_i$  from different realizations should be random, therefore, the numerator should be a summation of random variables to give an absolutely small value, that is, the bicoherence should be very close to zero. In contrast, the bicoherence should have a significant value if the waves are dependent and the phase

differences between three waves remain constant. Therefore, bicoherence is an indicator of the coupling strength between three elemental waves that satisfy the matching condition.

Figure 12 shows, for example, bicoherence diagrams obtained by the analysis of potential fluctuations measured with Langmuir probes at the plasma edge in JFT-2M and HL-2A. Note that the bicoherence analyses were applied to floating potential signals in JFT-2M and electric field signals in HL-2A. Both bicoherence diagrams clearly show the presence of two bright lines,  $f_1 + f_2 = f_3 = \pm 10$  kHz for JFT-2M [102, 104] and  $f_1 + f_2 = \pm 7$  kHz for HL-2A [105]. The third frequency,  $f_3$ , with a constant value, was shown to agree with the GAM frequencies in both the plasmas. Therefore, the two bright lines show that the nonlinear couplings between the GAM and the background turbulence are strong. A number of such experimental trials using bi-

coherence analysis have been made to prove that coupling occurs between GAMs and turbulence.

### 4.2 Bicoherence analysis in wavenumber and frequency

The matching condition in frequency shown in the previous subsection is a necessary condition but not sufficient condition for three wave couplings. In a strict sense, wavenumber matching must be evaluated as well, i.e.,  $\vec{k}_1 + \vec{k}_2 = \vec{k}_3$ , although wavenumber measurement is quite difficult in typical experimental conditions in toroidal plasmas, particularly in high-temperature plasmas. However, in a linear cylindrical devices, the LMD-U, a 64-channel azimuthal probe array succeeded in resolving the nonlinear couplings including the wavenumber space [106].

Figure 13 shows the bicoherence diagrams including wavenumber couplings in the poloidal direction. The 2D bicoherence diagram (in wavenumber and frequency) is difficult to fully illustrate, and three representative combinations in wavenumbers are shown in Fig. 13;  $(m_1, m_2, m_3) = (1, 1, 2)$ ,  $(m_1, m_2, m_3) = (1, 2, 3)$  and  $(m_1, m_2, m_3) = (5, 5, 10)$ . Several bright points indicate as the location of high bicoherence in the two diagrams at lower  $m$  numbers, revealing couplings between coherent modes, while the rest (higher mode numbers) shows the existence of broad regions with higher bicoherence values, indicating the couplings between rather broadband fluctuations.

### 4.3 Intermittency in wave couplings - wavelet bicoherence analysis

The intermittency is characteristic of turbulence. Hence, the couplings between elemental waves in turbulence could be intermittent. Bicoherence analysis based on Fourier transformation, however, cannot resolve this intermittency of nonlinear couplings. Moreover, it has been confirmed, as shown in Fig. 4, that the characteristics of turbulence change owing to the background structure of turbulence, i.e., zonal flows. The scale difference be-

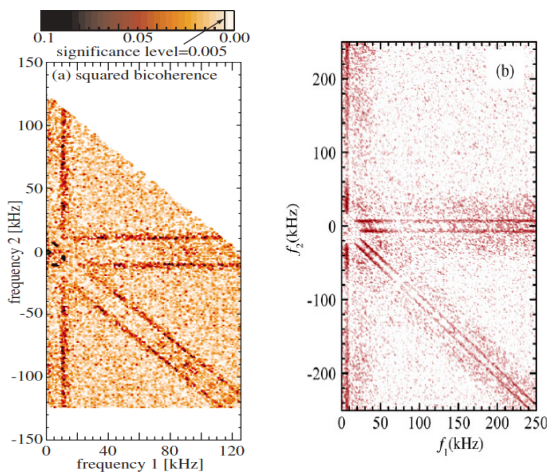


Fig. 12 Bicoherence analysis showing the couplings between GAM and turbulence in JFT-2M and HL-2A. (a) Bicoherence diagram in JFT-2M. The bicoherence value is high along the line  $f_1 + f_2 = \pm 10$  kHz, corresponding to the GAM frequency (Fig. 4, [102]). (b) Bicoherence diagram in HL-2A (Fig. 5, [105]).

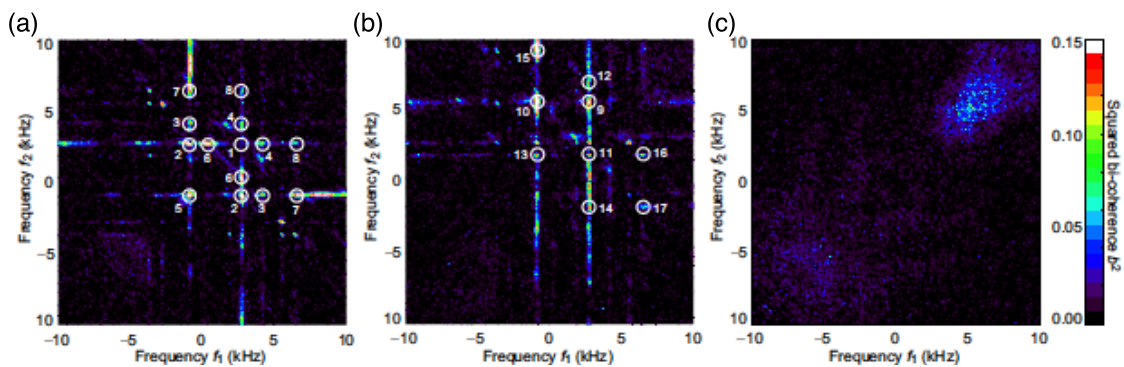


Fig. 13 Contour plots of squared bi-coherence,  $b^2$ , among three waves  $(m_1, f_1)$ ,  $(m_2, f_2)$ , and  $(m_3, f_3)$ , which satisfy the matching conditions  $(m_1, m_2, m_3) =$  (a) (1, 1, 2), (b) (1, 2, 3), and (c) (5, 5, 10). Circles with numbers indicate mode couplings (Fig. 6, [106]).

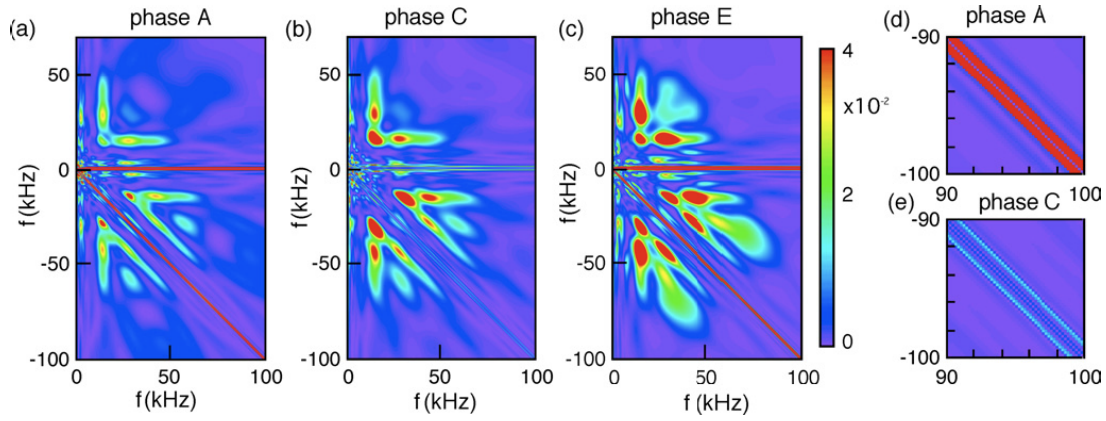


Fig. 14 Diagrams of wavelet squared bicoherence for three phases of zonal flow. Conditional average of wavelet bicoherence is calculated for five phases according to the magnitude of the zonal flow (see the text for details). Bicoherence diagrams of (a) phase A (maximum), (b) phase C (zero) and (c) phase E (minimum). Expanded views of the diagram for (d) phase A and (e) phase C (Fig. 2, [108]).

tween stationary zonal flows ( $\sim 0.5$  kHz) and turbulence ( $\sim 50$  kHz) could be  $\sim 100$ , thus, the turbulent properties can change during a change in the stationary zonal flows. Therefore, the nonlinear interactions between the component waves can be influenced by the condition of the stationary zonal flows, through mechanisms such as zonal flow shearing, wave scattering, and wave trapping [3].

Wavelet bicoherence analysis based on Morelet wavelets was invented to resolve the limitation of Fourier transformations described above [107]. The definition of the wavelet bicoherence is a simple extension of Eq. (15), and expressed as

$$b_w^2(\omega_1, \omega_2) = \frac{|\int \tilde{w}(\omega_1, t) \tilde{w}(\omega_2, t) \tilde{w}^*(\omega_3, t) dt|^2}{\int |\tilde{w}(\omega_1, t) \tilde{w}(\omega_2, t)|^2 dt \int |\tilde{w}(\omega_3, t)|^2 dt}, \quad (16)$$

where  $w_i(\omega, t)$  is the wavelet coefficient. As with bicoherence, the matching condition,  $f_3 = f_1 + f_2$ , should be satisfied.

In a CHS experiment, the wavelet bicoherence was used to evaluate the change in nonlinear couplings between the component waves for different phases of zonal flows [108]. Figure 14 shows the bicoherence diagrams calculated according to the following conditions of zonal flow direction relative to the bulk plasma flow; zonal flow velocity is maximum in the same direction as the bulk flow (phase A), maximum in the opposite direction (phase E), and nearly zero (phase C). Here, the number of the realizations is approximately  $\sim 20000$  for each diagram. The three bicoherence diagrams for the phases, A, C and E, reveal the strong dependence of the wave couplings of elemental waves in the turbulence on the zonal flow direction.

Several important findings should be mentioned. First, the couplings between elemental waves are obviously stronger as the zonal flow velocity decreases in the direction parallel to bulk flow. Second, the couplings are prominent along the lines of  $f_1 + f_2 \sim \pm 0.5$  kHz in phases A

(maximum) or E (minimum). The expanded views of one region ( $90 < |f| < 100$  kHz) clearly demonstrate that the couplings on the lines of  $f_1 + f_2 \sim \pm 0.5$  kHz strengthen as the zonal flow changes from phase C to phase A. The analysis proves the existence of the intermittent coupling between the stationary zonal flows and turbulence according to the zonal flow phase, which becomes prominent when the velocity of stationary zonal flows is at the minima and maxima.

Note that a large number of ensembles are necessary to obtain a statistically significant result in bicoherence analysis. In particular, a longer temporal window is required to obtain higher frequency resolution for treating extremely low frequency phenomena such as zonal flows. In other words, bicoherence analysis requires much longer discharges, or a number of identical shots for low-frequency phenomenon. However, wavelet bicoherence analysis can soften this statistically severe constraint. In fact, wavelet bicoherence analysis combined with the conditional average employed in the CHS experiment successfully resolves nonlinear three-wave couplings dependent on the zonal flow phase.

#### 4.4 Evaluation of internal energy transfer - Ritz's method

The power transfer function (PTF) method [109–113] was proposed to analyze the direction of energy transfer between component waves in turbulence. The method is based on a model equivalent to the Hasegawa-Mima equation [114], which can describe plasma turbulence concisely. The basic equation for this method in Fourier components of  $(k, \omega)$  is

$$\frac{\partial \phi(k, t)}{\partial t} = (\gamma_k + i\omega_k) \phi(k, t) + \frac{1}{2} \sum_{k_1, k_2, k_1+k_2=k} \Lambda_k^Q(k_1, k_2) \phi(k_1, t) \phi(k_2, t), \quad (17)$$

where  $\phi(k, t)$ ,  $\gamma_k$ ,  $\omega_k$  and  $\Lambda_k^Q(k_1, k_2)$  represent, the spatial Fourier spectrum of the fluctuating field, the growth rate, the dispersion relation and the coupling coefficient between wave components, respectively.

The equation can be modified to a form more suitable for expressing the energy transfer direction between the elemental waves in turbulence as follows,

$$\frac{\partial P_k}{\partial t} \simeq 2\gamma_k P_k + \sum T_k(k_1, k_2), \quad (18)$$

where  $T_k(k_1, k_2)$  represents the PTF from  $k_1$  and  $k_2$  to the wave  $k$ . The explicit form of the PTF is related to the coupling coefficient,  $\Lambda_k^Q(k_1, k_2)$ , as  $T_k(k_1, k_2) = \text{Re}[\Lambda_k^Q(k_1, k_2) \langle \phi_k^* \phi_{k_1} \phi_{k_2} \rangle]$ , where  $\text{Re}[\ ]$  denotes the operator for taking the real part.

In the actual analysis, the above coefficients are obtained by a finite difference equation between  $X_k = \phi(k, t)$  and  $Y_k = \phi(k, t + \tau)$ , which is derived from the above equation (see details in Ref. [109]). Using the calculus of finite differences, the equation, Eq. (17), can be reduced to an appropriate form for experimental analysis,

$$Y_k = L_k X_k + \frac{1}{2} \sum_{k_1, k_2} Q_k^{k_1, k_2} X_{k_1} X_{k_2}, \quad (19)$$

where  $L_k$  and  $Q_k^{k_1, k_2}$  are called the linear and quadratic non-linear functions, respectively. By multiplying and taking ensemble averages, we obtain

$$\begin{aligned} \langle Y_k X_k^* \rangle &= L_k \langle X_k X_k^* \rangle + \frac{1}{2} \sum_{k_1, k_2} Q_k^{k_1, k_2} \langle X_{k_1} X_{k_2} X_k^* \rangle, \\ \langle Y_k X_{k_1}^* X_{k_2}^* \rangle &= L_k \langle X_k X_{k_1}^* X_{k_2}^* \rangle \\ &\quad + \frac{1}{2} \sum_{k_1', k_2'} Q_k^{k_1', k_2'} \langle X_{k_1'} X_{k_2'} X_{k_1}^* X_{k_2}^* \rangle, \end{aligned} \quad (20)$$

where  $\langle X_k X_k^* \rangle$ ,  $\langle Y_k X_k^* \rangle$ ,  $\langle X_{k_2} X_{k_2}^* X_k^* \rangle$  and  $\langle Y_k X_{k_1}^* X_{k_2}^* \rangle$  are the auto-power, the cross-power, the auto-bicoherence, and the cross-bicoherence, respectively. The fourth-order term  $\langle X_{k_1} X_{k_2} X_{k_1}^* X_{k_2}^* \rangle$  must be calculated to obtain exact values of  $L_k$  and  $Q_k^{k_1, k_2}$ , which can be converted into a set of the coefficients,  $\gamma_k$ ,  $\omega_k$  and  $\Lambda_k^Q(k_1, k_2)$  (see Ref. [109]). However, to avoid a substantial computational load, the Millionshchikov's approximation is often adopted for the fourth-order term as  $\langle X_{k_1} X_{k_2} X_{k_1}^* X_{k_2}^* \rangle \simeq \langle |X_{k_1} X_{k_2}|^2 \rangle$ . The above-mentioned set of dependent equations is solved iteratively to provide the coefficients of the PTFs.

This method was applied to turbulence data for density fluctuations in the plasma edge region in the TEXT tokamak [109]. However, the wavenumber measurements required multipoint detection, which was difficult in actual experimental conditions. In the experiments, the density fluctuations were measured at two positions with Langmuir probes separated poloidally by  $\Delta x = 2$  mm and located 1 cm behind the limiter. The spectral analysis was performed on  $\phi(f, x)$  instead of  $\phi(k, t)$ , and requires the following transformations;  $t \rightarrow x, \tau \rightarrow \Delta x$ ,  $f \rightarrow k$ ,  $k \rightarrow f$ ,  $Y_k \rightarrow Y_f$ ,  $\omega_k \rightarrow k_f$ ,  $\gamma_k \rightarrow \gamma_f$ , and  $\Lambda_k^Q(k_1, k_2) \rightarrow \Lambda_f^Q(f_1, f_2)$ .

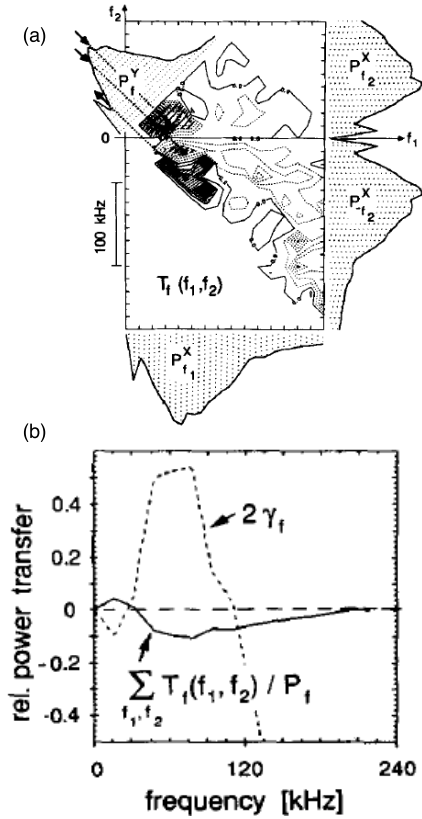


Fig. 15 Example of power transfer function (PTF) analysis from TEXT-U tokamak. (a) PTF. Solid and dashed lines represent positive and negative values, respectively. (b) Growth rate and normalized PTF as a function of frequency (Figs. 13 and 15, [109]).

The analysis successfully deduced the essential parameters, such as the dispersion relation  $k_f$ , the growth rate  $\gamma_f$  and PTF,  $T_f(f_1, f_2)$ , to demonstrate the presence of the cascading process. Figure 15 shows the power spectra at the two spatial points, the linear growth rate and the normalized total PTF. The results show that the modes in the frequency range from 30 to 110 kHz are linearly unstable, and the other modes are damped. The PTF in Fig. 15 illustrates the detailed process of the energy transfer direction between these modes, and supports the hypothesis that the fluctuation power should be transferred from the maximum power region around  $\sim 60$  kHz to stable regions, particularly the lower-frequency ranges of 10-40 kHz.

After this initial evaluation of the energy transfer, a modified energy transfer calculation procedure was applied to the BES fluctuation data in the Tokamak Fusion Test Reactor (TFTR). The results show that the global transport did not show a significant difference despite of the change in the energy transfer characteristics due to the variation in the toroidal plasma rotation [110, 111]. Moreover, PTF analysis in the H1 heliac showed that an inverse energy cascade from an unstable region to a stable region of lower frequency should occur to generate large coherent struc-

tures (see the following subsection) [112]. PTF analysis is extended and applied to 2D probe data, which provides turbulence information in the wavenumber space for the TJ-K torsatron. The energy transfer is evaluated in 2D wavenumber space, demonstrating a dual cascade feature of the inverse and forward directions in potential and density fluctuations, respectively [115]. The most recent work conducted in TJ-K along the above lines confirmed non-local energy transfer from drift waves to zonal flows [116].

Many other methods of inferring the energy transfer structure have been proposed, for example, energy transfer analysis based on a two-field model [117] and basis operator bispectral analysis [118]. Two-field model analysis includes the contribution of density fluctuations neglected in single-field models such as Ritz's and Kim's methods and has been applied to experimental data from TJ-K [119] and the Controlled Shear Decorrelation Experiment (CSDX) [120, 121]. In basis operator bispectral analysis the forms of energy transferred are prescribed as linear and nonlinear operators, and the coefficients of the operators for turbulence data are determined using the least squares methods. Furthermore, the cross-bicoherence analyses were used to evaluate the energy transfer between zonal flows and drift waves in the LMD-U [122], and to demonstrate the energy transfer mediated via GAM convection between density fluctuations in DIII-D [123].

### 4.5 Fluctuation envelope analyses for turbulence

The bicoherence technique can reveal a hidden link between wave components at different scales. Bicoherence analysis itself cannot resolve the energy transfer direction without any assumption regarding the equation that the system obeys. The amplitude correlation function (ACF) technique [124] uses a combination of numerical filtering and correlation functions to deduce the energy transfer direction between two components of different frequency regimes in turbulence spectra. In the ACF technique, the envelopes of the fluctuation components of relevant bands are obtained by numerical filtering. Then, the energy transfer direction is determined from the causal relation between the envelopes of the two components, assuming that the squares of the envelopes are proportional to the wave energy.

The cross-correlation function analysis of the envelopes of two fluctuations can be useful for determining the causality, as

$$C_{ACF}(\tau) = C_{crs}(Env(f_1(t)), Env(f_2(t))), \quad (21)$$

where  $f_1(t)$  and  $f_2(t)$  are the band-pass filtered signals of the relevant frequency ranges, and the operator  $Env[]$  denotes a function that takes the envelope, which may be low-pass filtered if necessary. The existence of a significant correlation indicates the presence of a causal relation between the two components, and the time delay or lag between two components indicates the direction of energy

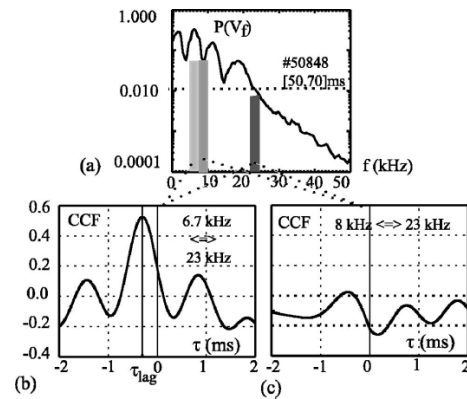


Fig. 16 Energy transfer analysis using the amplitude correlation function (ACF) technique in the H1 heliac. (a) Power spectrum of the floating potential fluctuation. Shading indicates the frequency ranges used in ACT analysis. (b) Correlation function between the envelopes of  $f \approx 6.7$  kHz (a peak) and  $f \approx 23$  kHz, and (c) correlation function between  $f \approx 8$  kHz (a trough) and  $f \approx 23$  kHz. The analysis demonstrates that unstable mode energy is transferred to the coherent structure at low frequencies (Fig. 7, [125]).

transfer. If the first component shows a delay relative to the second component, it is interpreted as that energy transfer is considered to occur from the second component to the first.

The example shown in Fig. 16 is from the data in the H1 heliac [112, 125]. The power spectrum (Fig. 16(a)) of the L-mode shows the existence of several coherent fluctuation structures represented by sharp peaks at low frequencies ( $f < 20$  kHz). PTF analysis indicates that the fluctuation energy of unstable higher-frequency regions ( $20 < f < 50$  kHz) is transferred to this low-frequency region. However, the rather poor frequency resolution up to 4 kHz, which is a trade-off for better statistics, cannot resolve the details of energy transfer between the coherent structures. The ACF technique successfully clarifies that the coherent structures are generated by energy transfer from unstable regions.

Here, the relationship between the peak frequency at  $f_1 = 6.7$  kHz and the unstable mode frequency ( $f_2 = 23$  kHz) and that between the trough frequency ( $f_1 = 8$  kHz) and the unstable frequency ( $f_2 = 23$  kHz) are examined. The former in Fig. 16(b) shows a significant correlation, and the negative time lag indicates that the energy transfer is directed from the unstable mode to the coherent mode. On the other hand, as is shown in Fig. 16(c), no significant correlation appears between the trough frequency and the unstable mode. Therefore, the ACF technique clearly demonstrates that the unstable mode energy is preferentially transferred into the coherent mode at low frequencies.

Moreover, as shown in Fig. 4, the turbulence observed in the electric field can be affected or modulated by zonal

flows, although the detailed mechanisms are not clearly identified. In the JFT-2M tokamak the envelope of density fluctuations of higher frequency is observed to be modulated by the GAM ( $\sim 10$  kHz), an oscillatory branch of zonal flows. Therefore, the presence of zonal flows or sheared flows is sensed or detected from modulations in the envelope of the density fluctuations which can be measured more easily than those of flows or the electric field [126, 127]. Therefore, this possibility of indirect measurement of zonal flows extends the opportunity for zonal flow experiments if the relationship between the zonal flows and the envelop modulation is completely understood.

## 5. Discussion - Interplay between Turbulence and Structure

### 5.1 Turbulence and thermal structure - flux generation

By enhancing transport, turbulence can work to reduce the inhomogeneity of thermal structures that cause plasma turbulence. If significantly correlated, two fluctuating physical quantities in turbulence can generate *fluxes* e.g., turbulence-driven particle, momentum and energy fluxes. These turbulence-driven fluxes are crucial for explaining anomalous transport in magnetically confined toroidal plasmas; cross-field transport in toroidal devices is well known to be anomalously large compared with that expected from collisional diffusion. Consequently, the turbulence and resultant fluxes strongly affect the structural formation of plasmas.

Anomalous transport has been ascribed to the transport arising from the cooperative works of fluctuations, that is, the finite values of temporal averages given by the cross-terms between the fluctuations of two physical quantities. For example, the particle flux can be described as  $\Gamma_r = \langle \tilde{n} \tilde{v}_r \rangle$ , where  $\tilde{n}$  and  $\tilde{v}_r$  are the density and velocity fluctuations, respectively. In magnetically confined low- $\beta$  plasmas, the dominant fluctuations are assumed to be electrostatic. Under this condition the velocity fluctuations should be those of  $E \times B$  drift, and the particle flux can be expressed as

$$\Gamma_r = \langle \tilde{n} \tilde{V} \rangle = \langle \tilde{n} (\tilde{E} \times B)_r \rangle B^{-2} = \langle \tilde{n} \tilde{E}_\theta \rangle B^{-1}, \quad (22)$$

Furthermore, the electric field fluctuation can be expressed as  $\tilde{E}_\theta = -\partial_\theta \tilde{\phi}$ , where  $\tilde{\phi}$  represents the potential fluctuations. The above expression is rewritten in an experimentally suitable form using Fourier expansion,

$$\begin{aligned} \Gamma_r &= \frac{1}{B} \sum_{\omega} k_\theta(\omega) \sqrt{P_n(\omega) P_\phi(\omega) \gamma_{n,\phi}(\omega)} \sin \phi(\omega) \Delta\omega \\ &= \frac{1}{B} \sum_{\omega} k_\theta(\omega) \text{Im}[P_{\text{crs}}](\omega) \Delta\omega \end{aligned} \quad (23)$$

where  $\text{Im}[P_{\text{crs}}]$  is the imaginary part of the cross power of density and potential fluctuations, and  $k_\theta$  is the poloidal wavenumber which can be obtained using the two-point

technique [128].

The cross-terms mentioned above have been evaluated using Langmuir probes in a number of the edge plasmas of toroidal devices [129, 130] and in low-temperature linear devices. In toroidal plasmas the particle fluxes were also evaluated using HIBPs in a few experiments [131]. Figure 17(a) shows the successful estimation of the turbulence-driven heat flux in the edge region of the TEXT tokamak as an example. The convected energy flux expressed as  $q_{\text{conv}} = T \Gamma_r$  is evaluated, and  $T$  is the temperature. A comparison of the evaluated flux with the experimental flux from the thermal equilibrium balance indicates that the convected energy flux should be sufficient to explain the amount of the heat transport in the plasma periphery.

In the above treatment using a Fourier transformation, the turbulence-driven fluxes are essentially assumed to be static. However, as shown in Fig. 6, particle transport is intermittent and dynamic, and a probabilistic treatment

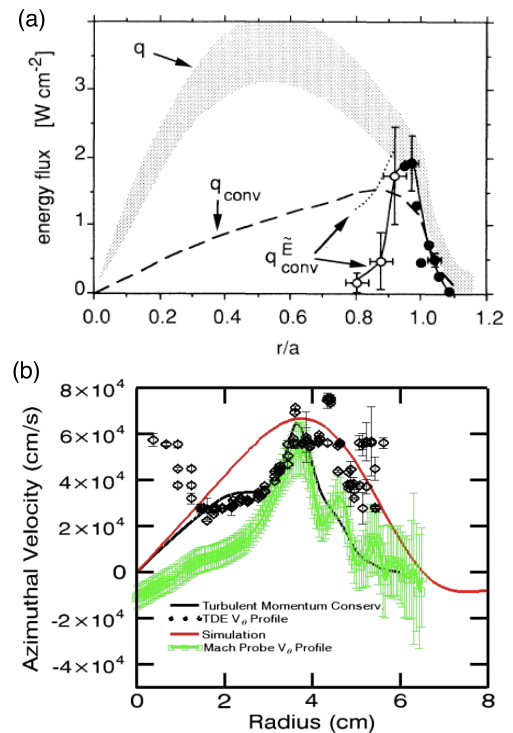


Fig. 17 (a) Radial profiles of the total electron and ion energy flux from the power balance (shaded area), the fluctuation-induced convected flux (closed circles from Langmuir probes; open circles from an HIBP) (Fig. 2, [129]). (b) Evaluation of turbulent Reynolds stress and poloidal flow generation in CDSX. Radial profiles of azimuthal velocity measured by time-delay estimation technique (TDE) (open diamonds) and Mach probe (open squares). Velocity profiles inferred from turbulent momentum balance analysis (red solid line) and predicted by collisional drift turbulence numerical simulation (solid line). Mach probe experimental errors show 95% confidence interval from least squares fitting. TDE error bars are determined from shot-to-shot scatter in the data (Fig. 6, [141]).

(PDF) may be a more appropriate approach for the modern view of turbulence. In such a treatment, the total flux crossing the poloidal surface, i.e., the integrated particle flux along the poloidal direction should be expressed as

$$\langle \Gamma_r(\theta) \rangle = \int \Gamma_r(\theta) P(\Gamma_r(\theta)) d\Gamma_r, \quad (24)$$

where the poloidal asymmetry of the fluctuations is assumed hence the poloidal angle  $\theta$  is included. Poloidal asymmetry in turbulence nature has been actually observed in axisymmetric systems such as tokamaks [132]. Therefore, in future the total turbulence-driven fluxes should be evaluated by the integration of the flux in the poloidal direction, considering the poloidal asymmetry of the fluxes.

## 5.2 Turbulence and electric field structure - flow generation

As is known in fluid mechanics, turbulence can induced momentum transfer or generate flows through the velocity cross-term,  $\langle v \nabla v \rangle$  i.e., the Reynolds stress term [133–136], as is analogous to the turbulence-driven flux. Note that the electric field is directly related to the velocity perpendicular to the magnetic field through  $E \times B$  drift in magnetically confined plasmas. Attempts have been made to measure the turbulent Reynolds stress in a number of devices, such as the ISTTOK tokamak [137], TJ-II stellarator [138], HT-6M ( $R = 0.65$  m  $a = 0.19$ ,  $B = 1$  T) [139] and the CASTOR tokamak [140], although 2D measurements of the local velocity or electric field are essential for the evaluation of turbulent Reynolds stress.

In addition to the measurements mentioned above, the momentum balance between the Reynolds stress drive and viscous damping was investigated in a linear cylindrical laboratory plasma, the CSDX [100, 141, 142]. In this experiment, the radial variation in the poloidal turbulent Reynolds stress term,  $\langle \tilde{v}_r \tilde{v}_\theta \rangle = \langle \tilde{E}_r \tilde{E}_\theta \rangle / B^2$ , was evaluated using a Langmuir probe array. Then the momentum balance equation below was solved in an equilibrium state ( $\partial/\partial t = 0$ ),

$$\begin{aligned} & \frac{1}{r^2} \frac{\partial}{\partial r} (r^2 \langle \tilde{v}_r \tilde{v}_\theta \rangle) \\ & = -\nu_{i-n} \langle v_\theta \rangle + \mu_{ii} \left( \frac{1}{r} \frac{\partial}{\partial r} \left( r \frac{\partial \langle v_\theta \rangle}{\partial r} \right) - \frac{\langle v_\theta \rangle}{r^2} \right) \end{aligned} \quad (25)$$

where the coefficients  $\nu_{i-n}$  and  $\mu_{ii}$  represent the ion-neutral collision rate and ion viscosity, respectively. With reasonable estimates of these coefficients, the equilibrium profile of the poloidal velocity was calculated. Figure 17(b) presents the measured poloidal flow profiles using time-delay-estimation (TDE) and Mach probes, the profile evaluated from the measured turbulent Reynolds stress, and a simulated profile resulting from a numerical calculation based on collisional drift turbulence. These profiles show good agreement.

In addition to turbulence-driven particle fluxes and Reynolds stress, dynamo effects observed in reversed field pinch (RFP) plasmas are another example of flux genera-

tion due to the cooperative works of turbulent fluctuations. In RFP plasmas, the reversed field of the magnetic configuration is spontaneously maintained for more than the resistive time. One possible mechanism is the generation of an electric field, which is derived from the generalized Ohm's law described as

$$E + \langle \tilde{v} \times \tilde{B} \rangle = \eta j, \quad (26)$$

where the second term on the left-hand side represents the cooperative works of the turbulent velocity and magnetic field fluctuations denoted  $\tilde{v}$  and  $\tilde{B}$ , respectively. A number of experiments have been performed to clarify the dynamo mechanisms observed in RFP plasmas [143–146].

Like turbulence-driven particle and heat fluxes, turbulence-driven momentum fluxes can be intermittent and poloidally asymmetric. Therefore, the treatment described in the previous section should also be necessary for turbulence-driven Reynolds stress or momentum fluxes. Moreover, it has been noted that particle flux asymmetry in the poloidal direction could drive poloidal plasma flows to compensate for the local excess or loss of particles (Stringer spin-up) [147, 148]. The mechanism suggests that the plasma flows should be considered essentially 3D. The importance of 3D observations of plasma flows or their driving mechanisms has been indicated in experiments in the JET [149] and TJ-II [150].

## 5.3 Impacts of sheared flows on turbulence

Experimental studies associated with transport barrier [151–154] have shown that sheared structure in flows or the electric field should play an important role in suppressing turbulence at transport barriers, as the initial theories for the H-mode suggested [155–158]. One famous example is the experimental examination of a forced transition to the H-mode using an externally biased electrode inserted into the plasma in the Continuous Current Tokamak (CCT) [159]. The plasma was observed to start rotating and to form an edge transport barrier, when a voltage was applied to the inserted electrode to generate a plasma potential. Later, this experiment of bias electrode was extended in the TEXTOR tokamak [160, 161]. The effect of shear suppression was clearly demonstrated in the bias-electrode experiments. The results show that the diffusive coefficient decreases as a function of generated electric field shear, supporting the theoretically predicted relation, i.e.,  $D \propto 1/(1 + \alpha E_r'^2)$ , where  $\alpha$  and  $E_r'$  represent a constant and the radial electric field shear, respectively.

Fundamental observations of the effects of shear flow on turbulence have been obtained in university experiments, taking advantage of their flexibility and accessibility [142, 162, 163]. In a cylindrical linear plasma at Kyushu University, sheared flow effects were observed in detail in an externally induced sheared flow by using the modulation of the plasma heating power [163]. In the device, a pressure-driven instability was observed in electron cyclotron resonance (ECR) heated plasma as a sharp peak

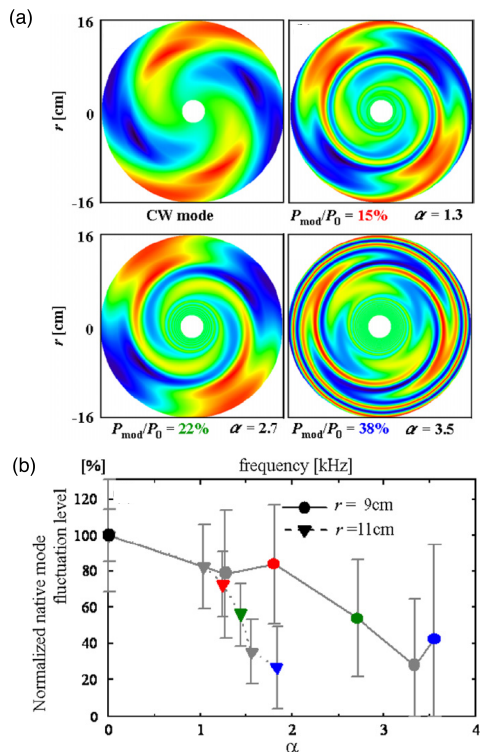


Fig. 18 Observation demonstrating the interplay between sheared flows and a pressure-driven mode in a linear cylindrical plasma. Sheared flow strength is controlled by the degree of the modulation of ECR heating. (a) Reconstructed images of the interplay between sheared flows and the mode. (b) Degree of suppression as a function of a parameter indicating shear flow strength,  $\alpha$  (Figs. 4 and 5, [163]).

in the fluctuation spectrum without any modulation of the ECR heating. With the application of ECR heating modulation, the sheared flows are induced, interacting with and suppressing the native mode. Figure 18 shows images of the changes in the reconstructed potential fluctuation patterns according to the modulation intensity of the heating power and the suppression ratio of the native mode as a function of the strength of the induced sheared flow. The results clearly demonstrate the alteration in the native mode as the shear flow strengthens, suggesting that three-wave coupling plays a role in the suppression.

Therefore, the experimental results show that turbulence should be affected by the flow structure, while the flows can be nonlinearly driven through Reynolds stress with turbulence. This nonlinear linkage between the flows and turbulence gives birth to the concept of a self-organized system of flows and turbulence. Based on this linkage, the prey and predator model [135] was proposed, where the L-mode and the H-mode should be regarded as two stable states for the system of flows and turbulence. Measurements in HT-6M, in fact suggested that the turbulent Reynolds stress should be the major driving force for the poloidal shear flows to induce their H-mode transition [139].

### 5.4 Causality - mutual interaction between turbulence and flows

The causal relationship between several events may often need to be clarified to allow investigation of the physical mechanisms of phenomena occurring in turbulent plasmas, for instance, the relationship between the electric field, the turbulence and the formation of a steep gradient at transport barrier. While turbulence can generate flow, turbulence should be affected by the generated background flows. Therefore, the mutual interaction between flows and turbulence provides an interesting causality problem. In such cases, it is useful to make Lissajous diagrams for related physical quantities. Statistical analysis using Lissajous diagrams was proposed to clarify causality problems for probabilistic phenomena [164].

Figure 19 shows an example of the proposed method applied to the competitive development of a drift wave [165], interchange mode and density gradient, which are observed in a linear cylindrical plasma. Lissajous diagrams for the relationship between the amplitudes of the interchange and drift modes are shown in Figs. 19 (b)–(d); two cycles of the Lissajous curves are extracted in Figs. 19 (c)–(d). The correlation coefficient,  $R$ , and the normalized area,  $A$ , are calculated as the characteristic parameters for each Lissajous (closed) curve. Note that the normalized area  $A$  has a sign, negative (clockwise) or positive (counterclockwise), to indicate the direction of development, i.e., which variable changes first.

In Fig. 19 (e)–(g), the statistic or distribution of  $(R, A)$  is shown for three combinations, i) drift wave vs. density gradient, ii) drift wave vs. interchange mode, and iii) interchange mode vs. density gradient. The analysis reveals that a concrete or close causal relation should exist between drift waves and the density gradient, however, no simple causal relation is expected for the other two combinations. The presence of two clumps in Figs. 19 (f) and (g) probably indicates that the interchange modes can change in two different ways in response to the development of the drift wave and density gradient, suggesting a hidden parameter controlling the appearance of the interchange mode.

A long-standing causality problem regarding transport barrier exists, stimulating the interests of many plasma scientists. The problem is whether the sheared flows (electric field) or the steep gradient is created first. Toroidal plasma experiments have confirmed that reduction of turbulence at the transport barriers is accompanied by sheared flows or a negative radial electric field, e.g., the early ones in DIII-D and JFT-2M [166, 167]. The radial force balance equation,  $(1/en_i)\partial p_i/\partial r = v_\theta B_\phi - v_\phi B_\theta + E_r$ , suggests that a negative radial electric field could be produced as the result of a steep pressure gradient at the barrier, assuming that the plasma velocity contribution is neglected.

Experiments have shown that the electric field is created first, before the transport barrier formation, in a few cases. A transition in the electric field was observed to

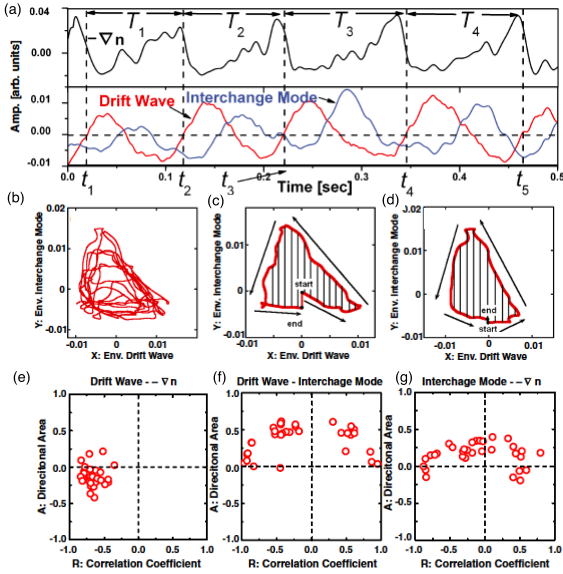


Fig. 19 (a) Time evolutions of envelopes of the drift wave (red) and the interchange mode (blue), and  $\nabla n$  (black), where the sampling time  $\Delta t = 1.0 \times 10^{-5}$  s. The period of the cycle of the drift wave envelope is the reference for dividing the time evolutions (dashed vertical lines). Lissajous diagrams between (X) the drift wave and (Y) the interchange mode for (b) one discharge time (1.0 s) and (c), and (d) one cycle (two samples).  $R - A$  plots for the relationships between (e) drift wave-density gradient [ $(\bar{R} = -0.67, \bar{A} = 0.13)$  and  $(\sigma_R^2 = 0.02, \sigma_A^2 = 0.02)$ ], (f) drift wave-interchange mode [ $(\bar{R} = -0.15, \bar{A} = 0.37)$  and  $(\sigma_R^2 = 0.38, \sigma_A^2 = 0.04)$ ], and (g) interchange mode-density gradient [ $(\bar{R} = -0.11, \bar{A} = 0.16)$  and  $(\sigma_R^2 = 0.25, \sigma_A^2 = 0.03)$ ]. Here, 32 ensembles are used (Figs. 1 and 2, [164]).

occur at a much faster timescale than confinement in internal transport barrier (ITB) formation of the CHS stellarator [168] and in the H-mode transition of JFT-2M using an HIBP [169]. Moreover, in an ITB in a stellarator [170–173], the formation of a positive radial electric field was found to deny the contribution of the pressure gradient to the barrier formation, since the increase in the pressure gradient results in increasing negative electric field. Therefore, the radial electric field formation obviously cannot be ascribed to the increase in the pressure gradient.

The transport barrier formation may not have a universal and single mechanism. The mechanism of barrier formation, or the causality between flows, turbulence, and pressure gradients should be examined for other cases of transport barrier formation and improved confinement modes. The method introduced in this section could be applied to oscillatory phenomena, such as edge localized modes, to investigate causality in transport barrier formation. The mechanisms of electric field generation or the causality should be a key concept in classifying transport barriers or improved confinement modes.

## 5.5 Mesoscale structure and transport

The synergetic efforts of theory, simulation and experiments have completed a paradigm shift in the recognition of plasma turbulence. The classical view regards plasma turbulence as an ensemble of drift waves, whereas in the modern view, plasma turbulence is a nonlinear system of drift waves and zonal flows. According to the modern view, zonal flows develop through energy transfer from the drift waves, and the saturation level of plasma turbulence is determined by the energy balance between the zonal flows and drift waves, as well as the shearing effect of zonal flows on the drift waves. The level of turbulent transport is reduced if the energy partition rate is high for zonal flows since the axisymmetric structure of zonal flows inhibits the accompanying cross-field transport.

Evidence for the role of energy partition between zonal flows and drift waves has been obtained in the observation of an ITB in the CHS stellarator [174]. As shown in Figs. 20 (a) and 20 (b), the zonal flow fraction clearly decreases at a location where a strong electric field shear existed with the barrier, after the back transition occurred. The high level of zonal flows should contribute to the transport improvement at the barrier. An unclear aspect of this transport barrier formation is that core plasma transport inside the barrier, where no sufficient electric field shear is generated, is also improved with the state of the transport barrier.

The energy partition between zonal flows and drift waves inside of the barrier has been examined; the conclusion was that the energy fraction of zonal flows is much higher in the state with a barrier than in the state without one. This higher fraction of zonal flows can be ascribed to the low damping rate of flows after a strong positive electric field is realized according to neoclassical bifurcation [175, 176]. This observation demonstrates that plasma transport is improved under conditions that enhance zonal flows, suggesting that a configuration with low flow damping should provide better confinement properties [177].

In contrast to zonal flows, it is also expected that the other extreme mesoscale structure, *streamers*, i.e., radially elongated and poloidally localized structures, should play an important role in core plasma transport. Although streamers have not been identified in toroidal plasmas, a simulation indicated that the interaction between zonal flows including GAMs and streamers or the interplay between mesoscale structures can be expected to affect the plasma transport and contribute to the structural formation of plasma [91]. In addition, the theories and simulations also predict that the collisionality should be a control parameter determining whether the plasma turbulence is dominated by streamers or zonal flows; the plasma turbulence should change from being dominated by streamers to being dominated by zonal flows as the collisionality decreases [69, 178, 179]. In regions of intermediate collisionality, the mutual interaction of zonal flows and streamers, similar to prey and predator behavior, is theoretically pre-

dicted [180]. The observation of such interactions should be an interesting goal on future experiments.

Moving from the plasma core to edge transport, it is universally found in a number of toroidal plasmas (including tokamaks and stellarators) that massive transport due to blob formation appears to be the dominant process governing edge transport. In cylindrical linear plasmas, as in toroidal plasmas, blob formation has been confirmed to show a PDF structure similar to those of toroidal plasmas. This circumstantial proof suggests that the intermittency commonly observed in both linear and toroidal plasmas could be ascribed to the appearance of blobs. In addition, according to an experiment at the ASDEX (see Fig. 6), a large fraction of the particle transport should be caused by the tail part of the PDF for turbulence-driven particle fluxes. This suggests the edge transport in toroidal plasma

could be governed by the massive transport arising from mesoscale structure, that is, blobs. The statistical features of edge transport, or structural transport accompanied by blobs should be investigated to clarify edge transport in toroidal plasmas.

### 5.6 Disparate-scale interaction and non-local transport and phenomena

Recent findings associated with plasma turbulence and transport give rise to a modern view in which the interactions between micro, meso and macroscale structures, or disparate-scale interactions determine plasma transport and structure. This concept may facilitate the understanding of unsolved problems in the physics of plasma transports e.g., the profile consistency [181] (or called resilience or stiffness), the presence of a critical gradient [182–184], the Dimits upshift [185], the co-existence of Bohm and gyro-Bohm behavior in transport [186–188], and nonlocal transport. Nonlocal transport observed in many devices [189–201] should be deeply related to the concept of disparate-scale interactions.

Figure 21 (a) illustrates a famous example of nonlocal transport, the cold pulse experiments in the TEXT. A cold pulse produced with pellet injection by external forced cooling at the edge propagates inward and triggers an increase in core electron temperature observed almost simultaneously at the moment of edge cooling [190]. It is not yet clear why the rapid change in plasma core transport began on a much shorter timescale than the confinement time or diffusive time necessary for the core plasma parameters to alter. Analogous to this phenomenon, the core temperature was observed to simultaneously rise at the moment of H-mode transition in the JET [191].

In this phenomenon, the change in microscale fluctuations governing core transport could be mediated through a

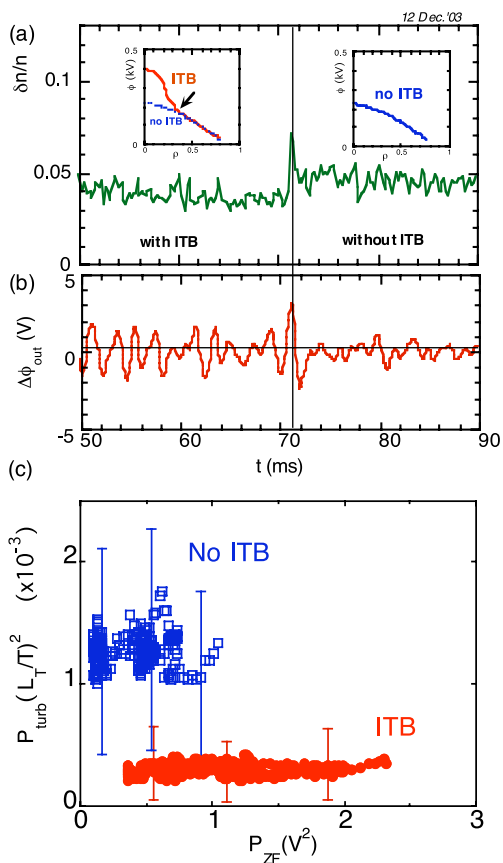


Fig. 20 Zonal flows and improved confinement in CHS. (a) Density fluctuation amplitude, and (b) zonal flow amplitude before and after a transition. Insets show potential profiles before and after the transition. Solid vertical line indicates the transition time. Arrow in the left inset indicates the point at which the fluctuations and zonal were observed. (c) Difference in energy partition between zonal flow and turbulence inside the barrier with and without a barrier. The turbulence is normalized by the electron temperature gradient to remove the effect of the change in driving force before and after the transition (Fig. 31, [4]).

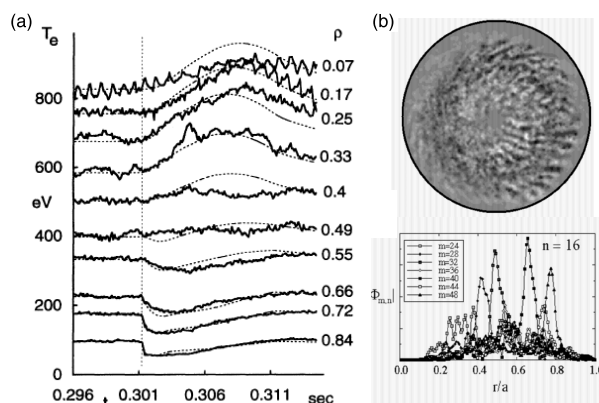


Fig. 21 (a) A famous example of nonlocal transport observed in the TEXT tokamak. Edge cooling with an injected pellet causes a simultaneous increase in core temperature (Fig. 2, [190]). (b) Example of simulation showing the wide-spreading structure produced by nonlinear multi-mode couplings in the saturation phase (Fig. 3, [203]).

structure with a longer characteristic length, which is also connected to the microscale fluctuations at the edge [202–209]. As shown in Fig. 21 (b), a simulation shows that multimode couplings produce a Bohm-scale structure covering a wide portion of plasmas in a nonlinear phase. This simulation result should be extended to the idea that a structure spreading over the plasma radius may be strongly coupled with micro-turbulence, such as zonal flows and drift waves, therefore, that local changes in microscale fluctuations may change the microscale fluctuations at distant locations through coupling with such a spreading mode. Zonal flows, which may have a long-distance correlation, have been confirmed to be pumped with drift waves, causing a back-reaction in the drift waves [122].

## 6. Summary

This paper presents turbulence phenomena, with an emphasis on methods of analyzing experimental data. The introduced phenomena include a number of nonlinear structures created and annihilated dynamically in plasma turbulence, e.g., zonal flows, streamers, blobs. The examined methods include Fourier spectral analysis, correlation analysis, wavelet analysis, bicoherence, PDF analysis, and conditional averaging. The use of these methods with advanced diagnostics has made it possible to visualize several hidden structures and their interrelationships.

The modern view of plasma turbulence established through the intensive efforts reviewed here is that a wide variety of creatures to which turbulence gives birth live in magnetized plasmas, competing and cooperating with each other to sustain their ecosystem - turbulence. These creatures may be short- or long-lived in time, large or small in size, and fast or slow in speed. In addition, a number of creatures still remain undiscovered. To realize fusion, we should know the characteristics of and the ways of interaction of these creatures, and design a proper environment surrounding them; a suitable magnetic configuration that provides a good confinement by controlling the population balance of the creatures.

For further understanding, the system of plasma turbulence should be minutely observed and carefully analyzed. For this purpose, experimental stages with high accessibility and flexibility must be essential. Low-temperature linear cylindrical devices have an important role in understanding very fundamental processes of plasma turbulence, although the realized turbulence may be less dynamic and have a fewer degrees of freedom compared to a toroidal plasma with confinement. It is desirable to construct a toroidal device not aiming at the high performance, but at high accessibility for observations that facilitate physical understanding of the plasma turbulence.

Finally, turbulence occurs in space and time. Therefore, fine measurements covering a sufficiently wide portion of a plasma, with fine temporal and spatial resolution, are needed to identify structures that have not yet been

seen, such as streamers in toroidal plasmas, and to observe the interplay between different scale structures, e.g., zonal flows, streamers and others. The highly developed modern computer technology, with advanced diagnostics and methods of analysis should make it possible to visualize the competition and cooperation between the structures at different scale and to establish the laws of structural formation in plasma turbulence.

## Acknowledgements

This paper is dedicated to Prof. Atsuo Iiyoshi, K. Itoh and S.-I. Itoh as an expression of my sincere appreciation for their continuous encouragements on the occasion of my winning the Inoue Prize for Science. The author is also grateful to Prof. K. Ida, K. Matsuoka, M. Yagi, and S. Inagaki, Drs. Y. Nagashima and T. Yamada for their fruitful discussion. This work was partially supported by Grant-in-aids for Scientific Research (No. 21224014).

- [1] P.C. Liewer, Nucl. Fusion **25**, 543 (1985).
- [2] A.J. Wootton, B.A. Carreras, H. Matsumoto *et al.*, Phys. Fluids B **2**, 2879 (1990).
- [3] P.H. Diamond, S.-I. Itoh, K. Itoh and T.S. Hahm, Plasma Phys. Control. Fusion **47**, R35 (2005).
- [4] A. Fujisawa, Nucl. Fusion **49**, 013001 (2009).
- [5] G.R. Tynan, A. Fujisawa and G. McKee, Plasma Phys. Control. Fusion **51**, 113001 (2009).
- [6] E. Mazzucato, Rev. Sci. Instrum. **69**, 2201 (1998).
- [7] T.P. Crowley, IEEE Trans. Plasma Sci. **22**, 291 (1994).
- [8] B. Bretz, Rev. Sci. Instrum. **68**, 2927 (1997).
- [9] A. Fujisawa, A. Shimizu, H. Nakano, S. Ohshima, K. Itoh *et al.*, J. Phys. Soc. Jpn. **76**, 033501 (2007).
- [10] A.D. Liu, T. Lan, C.X. Yu, H.L. Zhao *et al.*, Phys. Rev. Lett. **103**, 095002 (2009).
- [11] D.K. Gupta, R.J. Fonck, G.R. McKee, D.J. Schlossberg and M.W. Shafer, Phys. Rev. Lett. **97**, 125002 (2006).
- [12] E. Mazzucato, Phys. Rev. Lett. **36**, 792 (1976).
- [13] C.M. Surko and R.E. Slusher, Phys. Rev. Lett. **37**, 1747 (1976).
- [14] Y. Kawai, Y. Kiwamoto, Y. Soga and J. Aoki, Phys. Rev. E **75**, 066404 (2007).
- [15] Y. Kiwamoto, N. Hashizume, Y. Soga, J. Aoki and Y. Kawai, Phys. Rev. Lett. **99**, 115002 (2007).
- [16] Y. Kawai and Y. Kiwamoto, Phys. Rev. E **78**, 036401 (2008).
- [17] R.H. Kraichnan, Phys. Fluids **10**, 1417 (1967).
- [18] G.K. Batchelor, Phys. Fluids **12** (Suppl. II), 232 (1969).
- [19] P. Bak, C. Tang and K. Wiesenfeld, Phys. Rev. Lett. **59**, 381 (1987).
- [20] A. Hasegawa, Advanced Phys. **34**, 42 (1985).
- [21] A. Latten, T. Klinger, A. Piel and Th. Pierre, Rev. Sci. Instrum. **66**, 3254 (1995).
- [22] T. Yamada, Y. Nagashima, S. Inagaki *et al.*, Rev. Sci. Instrum. **78**, 123501 (2007).
- [23] H. Arakawa, K. Kamataki, S. Inagaki *et al.*, Plasma Phys. Control. Fusion **51**, 085001 (2009).
- [24] U. Stroth, F. Greiner, C. Lechte, N. Mahdizadeh, K. Rahbamia and M. Ramisch, Phys. Plasma **11**, 2558 (2004).
- [25] T. Yamada, S.-I. Itoh, T. Maruta *et al.*, Plasma Fusion Res. **2**, 051 (2007).

- [26] T. Yamada, S.-I. Itoh, T. Maruta *et al.*, *Nature Phys.* **4**, 721 (01 Sep. 2008).
- [27] T. Yamada, S.-I. Itoh and K. Terasaka, *Plasma Fusion Res.* **3**, S1021 (2008).
- [28] F. Zernike, *Physica (Utrecht)* **7**, 686 (1942).
- [29] R. Chatterjee, G.A. Hallock and A.J. Wootton, *Phys. Rev. Lett.* **82**, 2876 (1999).
- [30] In case that the property of the numerical filter,  $\tilde{h}(\omega)$ , is provided in the frequency domain, the kernel of the numerical filter is calculated as  $h(t) = \int \tilde{h}(\omega) \exp(i\omega t) d\omega$ , since the above transformation is expressed as  $\tilde{g}(\omega) = \tilde{h}(\omega)\tilde{f}(\omega)$  in the frequency domain.
- [31] M. Farge, K. Schneider and P. Devynck, *Phys. Plasmas* **13**, 042304 (2006).
- [32] R. Jha, P.K. Kaw, S.K. Mattoo, C.V.S. Rao, Y.C. Saxena and ADITYA team, *Phys. Rev. Lett.* **69**, 1375 (1992).
- [33] R.H. Kraichnan, *Phys. Rev. Lett.* **65**, 575 (1990).
- [34] R. Benzi, L. Biferale, G. Paladin, A. Vulpiani and M. Vergassola, *Phys. Rev. Lett.* **67**, 2299 (1991).
- [35] B.A. Carreras, B. van Milligen, M.A. Pedrosa *et al.*, *Phys. Rev. Lett.* **80**, 4438 (1998).
- [36] M. Endler, H. Niedermeyer, L. Giannone, E. Holzhauer, A. Rudyj, G. Theimer, N. Tsois and ASDEX team, *Nucl. Fusion* **35**, 1307 (1995).
- [37] R.A. Moyer, R.D. Lehmer, T.E. Evans, R.W. Conn and L. Schmitz, *Plasma Phys. Control. Fusion* **38**, 1273 (1996).
- [38] G. Antar, F. Gervais, P. Hennequin *et al.*, *Plasma Phys. Control. Fusion* **40**, 947 (1998).
- [39] B.A. Carreras, B. van Milligen, C. Hidalgo *et al.*, *Phys. Rev. Lett.* **83**, 3653 (1999).
- [40] G.Y. Antar, P. Devynck, X. Garbet and S.C. Luckhardt, *Phys. Plasmas* **8**, 1612 (2001).
- [41] B.A. Carreras, V.E. Lynch, D.E. Newman, R. Balbin, J. Bleuel, M.A. Pedrosa, M. Endler, B. van Milligen, E. Sánchez and C. Hidalgo, *Phys. Plasmas* **7**, 3278 (2000).
- [42] E. Sánchez, C. Hidalgo, D. López-Bruna *et al.*, *Phys. Plasmas* **7**, 1408 (2000).
- [43] J. Castellano, J.A. Jimenez, C. Hidalgo *et al.*, *Phys. Plasmas* **9**, 713 (2002).
- [44] P.H. Diamond and T.S. Hahm, *Phys. Plasmas* **2**, 3640 (1995).
- [45] G.Y. Antar, S.I. Krashninnkov, P. Devynck *et al.*, *Phys. Rev. Lett.* **87**, 065001 (2001).
- [46] A. Fujisawa, A. Shimizu, H. Nakano *et al.*, *Plasma Phys. Control. Fusion* **48**, S205 (2006).
- [47] N. Mahdizadeh, M. Ramisch, U. Stroth, C. Lechte and B.D. Scott, *Phys. Plasmas* **11**, 3932 (2004).
- [48] H. Johnsen, H.L. Pécseli and J. Trulsen, *Phys. Fluids* **30**, 2239 (1987).
- [49] A.V. Filippas, R.D. Bengston, G.-X. Li, M. Meier, Ch.P. Ritz and E.J. Powers, *Phys. Plasmas* **2**, 839 (1995).
- [50] O. Grulke, T. Klinger and A. Piel, *Phys. Plasmas* **6**, 788 (1999).
- [51] O. Grulke, T. Klinger, M. Endler, A. Piel and W7-AS Team, *Phys. Plasmas* **8**, 5171 (2001).
- [52] T.A. Carter, *Phys. Plasmas* **13**, 010701 (2006).
- [53] T. Windisch, O. Grulke and T. Klinger, *Phys. Plasmas* **13**, 122303 (2006).
- [54] S. Von Goeler, S.W. Stodiek and N. Sautoff, *Phys. Rev. Lett.* **33**, 1201 (1974).
- [55] H. Zohm, *Plasma Phys. Control. Fusion* **38**, 105 (1996).
- [56] K. McGuire *et al.*, *Phys. Rev. Lett.* **50**, 891 (1983).
- [57] C. Watts and R.F. Gandy, *Phys. Rev. Lett.* **75**, 1759 (1995).
- [58] S. Ohshima, A. Fujisawa, A. Shimizu *et al.*, *Plasma Phys. Control. Fusion* **49**, 1945 (2007).
- [59] K. Nagaoka, M. Isobe, K. Toi *et al.*, *Phys. Rev. Lett.* **100**, 065005 (2008).
- [60] S.J. Zweben, *Phys. Fluids* **28**, 974 (1985).
- [61] S. Benkadda, T. Dudok de Wit, A. Verga, A. Sen, ASDEX team and X. Garbet, *Phys. Rev. Lett.* **73**, 3403 (1994).
- [62] J.A. Boedo, D.L. Rudakov, R.A. Moyer *et al.*, *Phys. Plasmas* **10**, 1670 (2003).
- [63] S.H. Müller, A. Diallo, A. Fasoli *et al.*, *Phys. Plasmas* **13**, 100701 (2006).
- [64] I. Furno, B. Labit, M. Podesta *et al.*, *Phys. Rev. Lett.* **100**, 055004 (2008).
- [65] G.S. Xu, V. Naulin, W. Fundamenski, C. Hidalgo *et al.*, *Nucl. Fusion* **49**, 092002 (2009).
- [66] E. Martines, M. Hron and J. Stökel, *Plasma Phys. Control. Fusion* **44**, 351 (2002).
- [67] O. Grulke, J.L. Terry, B. LaBombard and S.J. Zweben, *Phys. Plasmas* **13**, 012306 (2006).
- [68] S.J. Zweben, R.J. Maqueda, D.P. Stotler *et al.*, *Nucl. Fusion* **44**, 134 (2004).
- [69] P.H. Diamond, *Nucl. Fusion* **41**, 1067 (2001).
- [70] K. Itoh, K. Hallatschek, S.-I. Itoh, P.H. Diamond and S. Toda, *Phys. Plasmas* **12**, 062303 (2005).
- [71] A. Fujisawa, K. Itoh, H. Iguchi *et al.*, *Phys. Rev. Lett.* **93**, 165002 (2004).
- [72] A. Fujisawa, K. Itoh, A. Shimizu *et al.*, *Phys. Plasmas* **15**, 055906 (2008).
- [73] G.S. Xu, B.N. Wan, M. Song and J. Li, *Phys. Rev. Lett.* **91**, 125001 (2003).
- [74] A. Fujisawa, T. Ido, A. Shimizu *et al.*, *Nucl. Fusion* **47**, S718 (2007).
- [75] Y. Hamada *et al.*, *Nucl. Fusion* **45**, 81 (2005).
- [76] T. Ido *et al.*, *Nucl. Fusion* **46**, 512 (2006).
- [77] Y. Nagashima *et al.*, *Plasma Phys. Control. Fusion* **48**, S1 (2006).
- [78] G.D. Conway, B. Scott, J. Schirmer, M. Reich, A. Kendl and the ASDEX-U team, *Plasma Phys. Control. Fusion* **47**, 1165 (2005).
- [79] G.D. Conway, C. Tröster, B. Scott, K. Hallatschek and the ASDEX-U team, *Plasma Phys. Control. Fusion* **50**, 055009 (2008).
- [80] A.V. Melnikov *et al.*, *Plasma Phys. Control. Fusion* **48**, S87 (2006).
- [81] M. Jakubowski, R.J. Fonck and G.R. McKee, *Phys. Rev. Lett.* **89**, 265003 (2002).
- [82] G.R. McKee *et al.*, *Plasma Phys. Control. Fusion* **45**, A477 (2003).
- [83] G.R. McKee, D.K. Gupta, R.J. Fonck, D.J. Scholossberg, M.W. Shafer and P. Gohil, *Plasma Phys. Control. Fusion* **48**, S123 (2006).
- [84] P.M. Schoch *et al.*, *Rev. Sci. Instrum.* **74**, 1846 (2003).
- [85] A. Fujisawa *et al.*, *Plasma Phys. Control. Fusion* **48**, S31 (2006).
- [86] M.G. Shats and W.M. Solomon, *Phys. Rev. Lett.* **88**, 045001 (2002).
- [87] K.J. Zhao, T. Lan, J.Q. Dong *et al.*, *Phys. Rev. Lett.* **96**, 255004 (2006).
- [88] L.W. Yan, J. Cheng, W.Y. Hong *et al.*, *Nucl. Fusion* **47**, 1673 (2007).
- [89] A. Krämer-Flecken, S. Soldatov, H.R. Koslowski, O. Zimmermann and TEXTOR Team, *Phys. Rev. Lett.* **97**, 045006 (2006).
- [90] A. Fujisawa, K. Itoh, A. Shimizu *et al.*, *Phys. Rev. Lett.*

- 98**, 165001 (2007).
- [91] P. Beyer, S. Benkadda, X. Barbet and P.H. Diamond, *Phys. Rev. Lett.* **85**, 4892 (2000).
- [92] N. Kasuya, M. Yagi, K. Itoh and S.-I. Itoh, *Phys. Plasmas* **15**, 052302 (2008).
- [93] M. Yagi, S.-I. Itoh, K. Itoh and P.H. Diamond, *Contrib. Plasma Phys.* **48**, 13 (2008).
- [94] P.A. Politzer, *Phys. Rev. Lett.* **84**, 1192 (2000).
- [95] Y. Hamada, T. Watari, A. Nishizawa *et al.*, *Phys. Rev. Lett.* **96**, 115003 (2006).
- [96] Y.C. Kim and E.J. Powers, *Trans. Plasma Sci.* **PS-7**, 120 (1979).
- [97] D. Brésillon and M.S. Hohamed-Benkadda, *Phys. Fluids* **31**, 1904 (1988).
- [98] C. Hidalgo, E. Sánchez, T. Estrada, B. Brañas and Ch.P. Ritz, *Phys. Rev. Lett.* **71**, 3127 (1993).
- [99] G.R. Tynan, R.A. Moyer, M.J. Burin and C. Holland, *Phys. Plasmas* **8**, 2691 (2001).
- [100] G.R. Tynan, R.A. Moyer, M.J. Burin and C. Holland, *Phys. Plasmas* **11**, 5195 (2004).
- [101] R.A. Moyer, J.R. Tynan, C. Holland and M.J. Burin, *Phys. Rev. Lett.* **87**, 135001 (2001).
- [102] Y. Nagashima *et al.*, *Phys. Rev. Lett.* **95**, 095002 (2005).
- [103] K. Itoh, Y. Nagashima, S.-I. Itoh, P.H. Diamond, A. Fujisawa, M. Yagi and A. Fukuyama, *Phys. Plasmas* **12**, 102301 (2005).
- [104] Y. Nagashima, S.-I. Itoh, M. Yagi *et al.*, *Rev. Sci. Instrum.* **77**, 045110 (2006).
- [105] T. Lan, A.D. Liu, C.X. Yu *et al.*, *Plasma Phys. Control. Fusion* **50**, 045002 (2008).
- [106] T. Yamada *et al.*, *Phys. Plasmas* **17**, 052313 (2010).
- [107] B.Ph. van Milligen, C. Hidalgo and E. Sánchez, *Phys. Rev. Lett.* **74**, 395 (1995).
- [108] A. Fujisawa, A. Shimizu, H. Nakano, S. Ohshima, K. Itoh *et al.*, *Plasma Phys. Control. Fusion* **49**, 211 (2007).
- [109] Ch.P. Ritz, E.J. Powers and R.D. Bengston, *Phys. Fluids B* **1**, 153 (1989).
- [110] J.S. Kim, R.D. Curst, R.J. Fonck *et al.*, *Phys. Plasmas* **3**, 3998 (1996).
- [111] J.S. Kim, R.J. Fonck, R.D. Durst, E. Fernandez, P.W. Terry, S.F. Paul and M.C. Zarnstorff, *Phys. Rev. Lett.* **79**, 841 (1997).
- [112] H. Xia and M.G. Shats, *Phys. Rev. Lett.* **91**, 155001 (2003).
- [113] Y. Nagashima, S.-I. Itoh, S. Shinohara, M. Fukao *et al.*, *Plasma Fusion Res.* **3**, 056 (2008).
- [114] A. Hasegawa and K. Mima, *Phys. Rev. Lett.* **39**, 205 (1977).
- [115] P. Manz, M. Ramisch, U. Stroth, V. Naulin and B.D. Scott, *Plasma Phys. Control. Fusion* **50**, 035008 (2008).
- [116] P. Manz, M. Ramisch and U. Stroth, *Phys. Rev. Lett.* **103**, 165004 (2009).
- [117] S.J. Camargo, D. Biskamp and B.D. Scott, *Phys. Plasmas* **2**, 48 (1995).
- [118] D.A. Baver, P.W. Terry and C. Holland, *Phys. Plasmas* **16**, 032209 (2009).
- [119] P. Manz, M. Ramisch and U. Stroth, *Plasma Phys. Control. Fusion* **51**, 035008 (2009).
- [120] M. Xu, G.R. Tynan, C. Holland, Z. Yan, S.H. Muller and J.H. Yu, *Phys. Plasmas* **16**, 042312 (2009).
- [121] M. Xu, G.R. Tynan, C. Holland, Z. Yan, S.H. Muller and J.H. Yu, *Phys. Plasmas* **17**, 032311 (2010).
- [122] Y. Nagashima, S.-I. Itoh, S. Shinohara *et al.*, *Phys. Plasmas* **16**, 020706 (2009).
- [123] C. Holland, G.R. Tynan, R.J. Fonck, G.R. McKee, J. Candy and R.E. Waltz, *Phys. Plasmas* **14**, 056112 (2007).
- [124] F.J. Crossley, P. Uddholm, P. Duncan, M. Khalid and M.G. Rusbridge, *Plasma Phys. Control. Fusion* **34**, 235 (1992).
- [125] H. Xia and M.G. Shats, *Phys. Plasmas* **11**, 561 (2004).
- [126] Y. Nagashima, K. Itoh, S.-I. Itoh, A. Fujisawa, M. Yagi *et al.*, *Plasma Phys. Control. Fusion* **49**, 1611 (2007).
- [127] K.J. Zhao, J.Q. Dong, L.W. Yan *et al.*, *Phys. Plasmas* **14**, 122301 (2007).
- [128] E.J. Powers, *Nucl. Fusion* **14**, 749 (1974).
- [129] Ch.P. Ritz, H. Lin, T.L. Rhodes and A.J. Wootton, *Phys. Rev. Lett.* **65**, 2543 (1990).
- [130] G.R. Tynan, L. Schmitz, R.W. Conn, R. Doerner and R. Lehmer, *Phys. Rev. Lett.* **68**, 3032 (1992).
- [131] G.A. Hallock, A.J. Wootton, R.L. Hickok and R.C. Isler, *Phys. Rev. Lett.* **59**, 1301 (1987).
- [132] A. Fujisawa, A. Ouroua, J.W. Heard, T.P. Crowley, P.M. Schoch, K.A. Connor and R.L. Hickok, *Nucl. Fusion* **36**, 375 (1996).
- [133] P.H. Diamond and Y.-B. Kim, *Phys. Fluids B* **3**, 1626 (1991).
- [134] J.F. Drake, J.M. Finn, P. Guzdar *et al.*, *Phys. Fluids B* **4**, 488 (1992).
- [135] P.H. Diamond, Y.-M. Liang, B.A. Carreras and P.W. Terry, *Phys. Rev. Lett.* **72**, 2565 (1994).
- [136] P.N. Guzdar, *Phys. Plasmas* **2**, 4174 (1995).
- [137] C. Hidalgo, C. Silva, M.A. Pedrosa, E. Sánchez, H. Fernandes and C.A.F. Varandas, *Phys. Rev. Lett.* **83**, 2203 (1999).
- [138] C. Hidalgo, M.A. Pedrosa, E. Sánchez *et al.*, *Plasma Phys. Control. Fusion* **42**, A153 (2000).
- [139] Y.H. Xu *et al.*, *Phys. Rev. Lett.* **84**, 3867 (2000).
- [140] M. Vergote, M. Van Schoor, Y. Xu, S. Jachmich and R. Weynants, *Plasma Phys. Control. Fusion* **48**, S75 (2006).
- [141] G.R. Tynan, C. Holland, J.H. Yu, A. James, D. Nishijima, M. Shimada and N. Taheri, *Plasma Phys. Control. Fusion* **48**, S51 (2006).
- [142] C. Holland, J.H. Yu, A. James, D. Nishijima, M. Shimada, N. Taheri and G.R. Tynan, *Phys. Rev. Lett.* **96**, 195002 (2006).
- [143] H. Ji, H. Toyama, A. Fujisawa, S. Shinohara and K. Miyamoto, *Phys. Rev. Lett.* **27**, 616 (1992).
- [144] H. Ji, Y. Yagi, K. Hattori *et al.*, *Phys. Rev. Lett.* **75**, 1086 (1995).
- [145] E. Martines and F. Vallone, *Phys. Rev. E* **56**, 957 (1997).
- [146] L. Frassinetti, I. Predebon, H. Koguchi *et al.*, *Phys. Rev. Lett.* **97**, 175001 (2006).
- [147] T.E. Stringer, *Phys. Rev. Lett.* **22**, 1770 (1969).
- [148] A.B. Hassam, T.M. Antonsen Jr., J.F. Drake and C.S. Liu, *Phys. Rev. Lett.* **80**, 5353 (1998).
- [149] C. Hidalgo, B. Gonçalves, C. Silva *et al.*, *Phys. Rev. Lett.* **91**, 065001 (2003).
- [150] B. Gonçalves, C. Hidalgo, M.A. Pedrosa, R.O. Orozco, E. Sanchez and C. Silva, *Phys. Rev. Lett.* **96**, 145001 (2006).
- [151] K. Itoh and S.-I. Itoh, *Plasma Phys. Control. Fusion* **38**, 1 (1996).
- [152] K.H. Burrell, *Phys. Plasmas* **4**, 1499 (1997).
- [153] J.W. Connor and H.R. Wilson, *Plasma Phys. Control. Fusion* **42**, R1 (2000).
- [154] A. Fujisawa, *Plasma Phys. Control. Fusion* **45**, R1 (2003).
- [155] F. Wagner, G. Becker, K. Behringer *et al.*, *Phys. Rev. Lett.* **49**, 1408 (1982).
- [156] ASDEX Team, *Nucl. Fusion* **29**, 1959 (1989).

- [157] S.-I. Itoh and K. Itoh, *Phys. Rev. Lett.* **60**, 2276 (1988).
- [158] K.C. Shaing and E. Crume Jr., *Phys. Rev. Lett.* **63**, 2369 (1989).
- [159] R. Taylor *et al.*, *Phys. Rev. Lett.* **63**, 2365 (1989).
- [160] R.R. Weynants, G. Van Oost, G. Bertschinger *et al.*, *Nucl. Fusion* **32**, 837 (1992).
- [161] R.R. Weynants, S. Jachmich and G. Van Oost, *Plasma Phys. Control. Fusion* **40**, 635 (1998).
- [162] T. Kaneko, H. Tsunoyama and R. Hatakeyama, *Phys. Rev. Lett.* **90**, 125001 (2003).
- [163] H. Tsuchiya, S.-I. Itoh, A. Fujisawa, K. Kamataki, S. Shinohara, M. Yagi, Y. Kawai, A. Komori and K. Itoh, *Plasma Phys. Control. Fusion* **50**, 055005 (2008).
- [164] K. Kamataki, K. Itoh, S.-I. Itoh, A. Fujisawa, S. Inagaki, Y. Nagayama, M. Yagi and T. Yamada, *J. Phys. Soc. Jpn.* **79**, 024501 (2010).
- [165] K. Kamataki, S.-I. Itoh, Y. Nagashima, S. Inagaki *et al.*, *Plasma Phys. Control. Fusion* **50**, 035011 (2008).
- [166] R.J. Groebner, K.H. Burrell and R.P. Seraydarian, *Phys. Rev. Lett.* **64**, 3015 (1990).
- [167] K. Ida, S. Hidekuma, Y. Miura, T. Fujita, M. Mori, K. Hoshino, N. Suzuki, T. Yamauchi and JFT-2M Group, *Phys. Rev. Lett.* **65**, 1364 (1990).
- [168] A. Fujisawa, H. Iguchi, H. Sanuki *et al.*, *Phys. Rev. Lett.* **79**, 1054 (1997).
- [169] T. Ido, K. Kamiya, Y. Miura *et al.*, *Phys. Rev. Lett.* **88**, 055006 (2002).
- [170] A. Fujisawa *et al.*, *Phys. Rev. Lett.* **82**, 2669 (1999).
- [171] U. Stroth *et al.*, *Phys. Rev. Lett.* **86**, 5910 (2001).
- [172] C. Alejaldre *et al.*, *Nucl. Fusion* **41**, 1449 (2001).
- [173] K. Ida, T. Shimozuma, H. Funaba *et al.*, *Phys. Rev. Lett.* **91**, 085003 (2003).
- [174] K. Itoh, S. Toda, A. Fujisawa *et al.*, *Phys. Plasmas* **14**, 020702 (2007).
- [175] L.M. Kovrizhnykh, *Nucl. Fusion* **24**, 435 (1984).
- [176] D.E. Hastings, *Phys. Fluids* **27**, 935 (1984).
- [177] A. Fujisawa, *Plasma Fusion Res.* **5**, S1005 (2010).
- [178] A. Das, A. Sen, S. Mahajan and P. Kaw, *Phys. Plasmas* **8**, 5104 (2001).
- [179] N. Kasuya *et al.*, *Phys. Plasmas* **15**, 052302 (2008).
- [180] S.-I. Itoh and K. Itoh, *Plasma Phys. Control. Fusion* **50**, 055002 (2008).
- [181] B. Coppi, *Comments Plasma Phys. Control. Fusion* **5**, 261 (1980).
- [182] C.C. Petty, M.R. Wade, J.E. Kinsey, R.J. Groebner, T.C. Luce and G.M. Staebler, *Phys. Rev. Lett.* **83**, 3661 (1999).
- [183] G.T. Hoang, C. Bourdelle, X. Garbet, G. Giruzzi, T. Aniel and M. Ottaviani, *Phys. Rev. Lett.* **87**, 125001 (2001).
- [184] F. Ryter, F. Leuterer, G. Pereverzev, H.-U. Fahrback, J. Sober, W. Suttrup and ASDEX Upgrade Team, *Phys. Rev. Lett.* **86**, 2325 (2001).
- [185] A.M. Dimits, G. Bateman, M.A. Beer *et al.*, *Phys. Plasmas* **7**, 969 (2000).
- [186] R.E. Waltz, J.C. DeBoo and M.N. Rosenbluth, *Phys. Rev. Lett.* **65**, 2390 (1990).
- [187] U. Stroth, G. Kühner, H. Maassberg, H. Ringler and W7-AS Team, *Phys. Rev. Lett.* **70**, 936 (1993).
- [188] C.C. Petty, T.C. Luce, R.I. Pinsky *et al.*, *Phys. Rev. Lett.* **74**, 1763 (1995).
- [189] T. Luce, C.C. Petty and J.C.M. de Haas, *Phys. Rev. Lett.* **68**, 52 (1992).
- [190] K.W. Gentle *et al.*, *Phys. Rev. Lett.* **74**, 3620 (1995).
- [191] J.G. Cordey, B. Balet, D.V. Barlett *et al.*, *Nucl. Fusion* **39**, 301 (1999).
- [192] N.J. Lopes Cardozo, *Plasma Phys. Control. Fusion* **37**, 799 (1995).
- [193] M.W. Kissick, J.D. Callen, E.D. Fredrickson, A.C. Janos and G. Taylor, *Nucl. Fusion* **36**, 1691 (1996).
- [194] P. Galli, A. Cherubini, R. de Angelis *et al.*, *Nucl. Fusion* **38**, 1355 (1998).
- [195] P. Mantica, P. Galli, G. Gorini, G.M.D. Hogewij, J. de Kloe, N.J. Lopes Cardozo and RTP team, *Phys. Rev. Lett.* **82**, 5048 (1999).
- [196] P. Galli, G. Gorini, P. Manica, G.M.D. Hogewij, J. de Kloe, N.J. Lopes Cardozo and RTP team, *Nucl. Fusion* **39**, 1355 (1999).
- [197] B.P. van Milligen, E. de la Luna, F.L. Tabarés *et al.*, *Nucl. Fusion* **42**, 787 (2002).
- [198] S. Inagaki, K. Ida, N. Tamura *et al.*, *Plasma Phys. Control. Fusion* **46**, A71 (2004).
- [199] S. Inagaki, H. Takenaga, K. Ida *et al.*, *Nucl. Fusion* **46**, 133 (2006).
- [200] S. Inagaki, N. Tamura, T. Otkuzawa *et al.*, *Plasma Phys. Control. Fusion* **48**, A251 (2006).
- [201] N. Tamura, S. Inagaki, K. Tanaka *et al.*, *Nucl. Fusion* **47**, 449 (2007).
- [202] X. Garbet, L. Laurent, A. Samain and J. Chinardet, *Nucl. Fusion* **34**, 963 (1994).
- [203] R.D. Sydora, V.K. Decyk and J.M. Dawson, *Plasma Phys. Control. Fusion* **38**, A281 (1996).
- [204] S.E. Parker, H.E. Mynick, M. Artun, J.C. Cummings, V. Decyk, J.V. Kepner, W.W. Lee and W.M. Tang, *Phys. Plasmas* **3**, 1959 (1996).
- [205] L. Chen, R.B. White and F. Zonca, *Phys. Rev. Lett.* **92**, 075004 (2004).
- [206] F. Zonca, R.B. White and L. Chen, *Phys. Plasmas* **11**, 2488 (2004).
- [207] T.S. Hahm, P.H. Diamond, Z. Lin, K. Itoh and S.-I. Itoh, *Plasma Phys. Control. Fusion* **46**, A323 (2004).
- [208] R.E. Waltz and J. Candy, *Phys. Plasmas* **12**, 072303 (2005).
- [209] S.-I. Itoh and K. Itoh, *Plasma Phys. Control. Fusion* **43**, 1055 (2001).